

This is an Open Access document downloaded from ORCA, Cardiff University's institutional repository:<https://orca.cardiff.ac.uk/id/eprint/134655/>

This is the author's version of a work that was submitted to / accepted for publication.

Citation for final published version:

Loza Espejel, Roberto , Alves, Tiago M. and Blenkinsop, Tom G. 2020. Multi-scale fracture network characterisation on carbonate platforms. *Journal of Structural Geology* 140 , 104160. 10.1016/j.jsg.2020.104160

Publishers page: <http://dx.doi.org/10.1016/j.jsg.2020.104160>

Please note:

Changes made as a result of publishing processes such as copy-editing, formatting and page numbers may not be reflected in this version. For the definitive version of this publication, please refer to the published source. You are advised to consult the publisher's version if you wish to cite this paper.

This version is being made available in accordance with publisher policies. See <http://orca.cf.ac.uk/policies.html> for usage policies. Copyright and moral rights for publications made available in ORCA are retained by the copyright holders.



1 **Multi-scale fracture network characterisation on carbonate platforms**

2 Roberto Loza Espejel*, Tiago M. Alves and Tom G. Blenkinsop

3 3D Seismic Lab, School of Earth and Ocean Sciences, Cardiff University, Main Building –
4 Park Place, CF10 3AT, Cardiff, United Kingdom

5 *Corresponding author:

6 Mobile phone: +44 7479 746160.

7 E-mail address: lozaespejelr@cardiff.ac.uk and lozaespejelr@gmail.com

8 **Keywords:** fracture networks; topology; geometry; outcrop analogue; carbonate platforms;
9 fractured reservoirs

10 **Abstract**

11 Characterisation of fracture networks at different scales is challenging and important to
12 many fields of geoscience, especially when access to multiple resolution datasets is limited.
13 Here, we develop an integrated analysis of fracture networks on carbonate platforms using
14 three scales of observation: small (outcrop), intermediate (airborne LiDAR) and large (3D
15 seismic). Statistical analyses and ternary diagrams of geometrical and topological data from
16 Cariatiz (South East Spain) and Pernambuco (East Brazil) are used to understand the
17 relationships and distribution of fracture networks between multi-scale datasets. A variety of
18 fracture types at each scale of observation reveal how complex fracture networks are on
19 carbonate platforms. Our results demonstrate that fracture network properties behave
20 differently depending on the fracture size, and that transitional scale gaps between datasets
21 constrain fracture characterisation. Airborne LiDAR maps show that intermediate-sized
22 fractures appear to have a better controlled orientation and a lower connectivity than smaller
23 fractures from the same area in Cariatiz. Fracture branch length distributions fit a negative

24 exponential or log-normal distribution for massive non-stratabound units. This work is
25 important as it demonstrates that the use of outcrop data is a good approach to understand
26 fracture complexity of carbonate platforms. Understanding sub-seismic fracture networks is
27 therefore critical in quantifying fluid flow and permeability in carbonate reservoirs.

28 **1 Introduction**

29 Fracture networks control many physical properties in rocks, and their characterisation
30 is important in many disciplines of geosciences and engineering, including oil and gas
31 exploration (Nelson, 2001; Sarkheil et al., 2013), geothermal reservoir characterisation (Chen
32 et al., 2018; TerHeege et al., 2018; Vidal and Genter, 2018; Doornenbal et al., 2019), carbon
33 capture and storage projects (March et al., 2018), hydrogeology and environmental geology
34 studies (Abotalib et al., 2019; Medici et al., 2019), as well as mining and tunnelling (Friedman,
35 1975; Van As and Jeffrey, 2002; Zarei et al., 2012). Fracture networks have a significant effect
36 on porosity, permeability and fluid flow of naturally fractured units. Well-connected open
37 fractures can increase the natural permeability of rocks to provide active conduits for fluid flow
38 (Laubach, 2003; Maerten et al., 2006; Strijker et al., 2012; Gutmanis et al., 2018). Conversely,
39 closed or cemented fractures can act as barriers compartmentalising reservoirs, which is
40 important for field delineation (Bourbiaux, 2010). Examples of fractured carbonate reservoirs
41 can be found worldwide including the Cantarell complex in Campeche (Gulf of Mexico), the
42 Haft Kel field in North Iraq (Middle East), and the Ekofisk complex in the North Sea
43 (Dominguez et al., 1992; Key et al., 1999; Hermansen et al., 2000; Alavian and Whitson, 2005;
44 Mandujano et al., 2005; Bourbiaux, 2010; Santiago et al., 2014; Galvis, 2018).

45 A key aspect in reservoir characterisation is the need to analyse the interaction between
46 individual fractures and fracture sets, which can be estimated by studying topological attributes
47 such as branch and node types (Strijker et al., 2012; Sanderson and Nixon, 2015). Both
48 geometrical and topological attributes affect the connectivity and permeability of a rock

49 volume. Moreover, natural fractures typically occur over several orders of magnitude; they
50 range from microscopic fissures to kilometre structures such as fracture swarms or corridors
51 (Bush, 2010). It is therefore crucial to understand the scale dependency of these distribution
52 parameters to characterise sub-surface fluid flow patterns (Berkowitz, 2002; Tao and Alves,
53 2019).

54 Fractures can be described by quantifiable geometrical attributes such as their orientation,
55 length, height, spacing, morphology, or some other form of classification involving fracture
56 type and mineral fill (Odling et al., 1999). In this paper, we use the term *fracture* for any type
57 of discontinuity (joints, faults, etc.) formed in different settings, such as during large-scale
58 tectonic events, local uplift and erosion, slope instability or excess fluid pressure (Peacock et
59 al., 2000, 2016; Berkowitz, 2002; Kim and Sanderson, 2005). The intention is to characterise
60 an entire fracture network, including different fracture types of various sizes that interact
61 between each other within a given rock unit, as all of them may contribute to the connectivity
62 of the fracture network. Specific terms such as fault, joint, fracture swarm, etc. are only used
63 where the fracture type and geological connotation are important to the analysis.

64 *1.1 Challenges and limitations*

65 One of the main challenges when characterising fracture networks is to obtain reliable
66 data to analyse fracture networks at different scales. At present, it is still difficult to fully
67 characterise fractures from a single dataset or by utilising data in which fractures of certain
68 sizes cannot be observed due to limited data resolution. Integration of datasets and the
69 knowledge of the capabilities for each type of data are key. Ideally, a carbonate platform with
70 access to an exhaustive dataset, allowing mapping at different scales in both surface (e.g.
71 outcrop mapping, drone imagery, airborne LiDAR) and sub-surface (e.g. cores, borehole,
72 seismic), would provide a comprehensive setting to fully characterise not just fracture
73 networks, but also additional structural and sedimentological properties. However, availability

74 of such a perfect scenario is rare, and the necessity to work with limited datasets is a daily issue
75 for geoscientists.

76 Three-dimensional (3D) reflection seismic data is usually the main source of subsurface
77 structural information in industry. Seismic surveys are generally acquired at a line spacing of
78 25 to 50 m and, depending on the resolution of the seismic volume, faults with throws smaller
79 than 10 to 30 m cannot be resolved (Needham et al., 1996; Lohr, 2004; Maerten et al., 2006).
80 Faults and fractures of sizes below seismic resolution, referred to as sub-seismic, can only be
81 determined using borehole data (e.g. wireline logs, cores, well log images), leading to
82 underestimations of fracture volumes (Maerten et al., 2006). Fracture downscaling or upscaling
83 using discrete stochastic methods is a common practice to populate fractures with a scale that
84 cannot be observed directly from the studied dataset, for example between seismic and
85 borehole data (Cacas et al., 2001; Chilès, 2005). Similarly, fractal analyses have been
86 undertaken to characterise fracture properties (Needham et al., 1996; Nicol et al., 1996; Bonnet
87 et al., 2001). However, their scale invariance is still subject to controversy (Cowie et al., 1996;
88 Needham et al., 1996; Nicol et al., 1996; Gillespie et al., 2001; Guerriero et al., 2010), and
89 extrapolations with limited reliable statistics can lead to important uncertainties (Maerten et
90 al., 2006).

91 Outcrop analogues play an important role in the evaluation of small- and intermediate-
92 scale fracture parameters that cannot be quantified from seismic and borehole data (e.g. Eberli
93 et al., 2005; Gutmanis et al., 2018, Fig.4). Field analogues can guide the development of
94 conceptual reservoir models and provide spatial and statistical data to understand inter-well
95 fracture property populations, as techniques are available to cover all scales of observation
96 (Nelson, 2001; Strijker et al., 2012; Gutmanis and Ardèvol i Oró, 2015; Sanderson, 2016). In
97 such analyses, it is important to carefully choose valid field analogues to calibrate them with
98 reservoir data (Cacas et al., 2001; Laubach et al., 2009; Kleipool et al., 2017). If there is

99 sufficient exposure of fracture data, and sampling is undertaken carefully using appropriate
100 methodologies (e.g. circular scanlines), field analogues can provide valuable information to
101 characterise 3D fracture networks in multi-scale scenarios (Bertotti et al., 2007; Strijker et al.,
102 2012).

103 This study is not an exception of the challenges associated to data limitations; in fact, we
104 aim to emphasise the issues associated when characterising multi-scale fracture networks. For
105 this reason, an integrated methodology is explained in detail, utilising three scales of
106 observation from two carbonate platforms with similar settings. This approach allowed us to
107 characterise fractures at sub-seismic (centimetre to metre) and seismic (kilometre) scales.

108 The Cariatiz carbonate platform in the Sorbas Basin, SE Spain, which has a unique 3D
109 exposure, was used to analyse the geometry and topology of fracture networks at two sub-
110 seismic scales from outcrop mapping (small scale) and airborne LiDAR (Light Detection and
111 Ranging) maps (intermediate scale) (Fig. 1). Correlating the two datasets, covering the same
112 carbonate platform, allowed us to predict trends of fracture properties at different scales. In
113 addition, three-dimensional (3D) seismic studies from the Pernambuco carbonate platform in
114 East Brazil were used to analyse km-long fracture networks (Fig. 2). Comparison between the
115 two study areas (Cariatiz and Pernambuco) have limitations as they are not in the same region.
116 However, they are of great importance to improve the understanding of multi-scale fracture
117 networks (Fig. 3). Outcrop data provides the opportunity to understand sub-seismic fractures
118 that can be used as conceptual models when only working with seismic data. In contrast,
119 seismic data is useful to understand km-long fractures that are often poorly exposed, and can
120 also be used as conceptual models for example, when working with borehole data or surface
121 data.

122 This study is a novel approach to study multi-scale fracture networks. However, there is
123 indeed the possibility and a call to continue future work to test and apply our observations and
124 conclusions in similar carbonate platforms which might have a more robust dataset covering
125 fracture sizes of several orders of magnitude in the same region. This paper addresses the
126 following research questions:

- 127 a) How can we improve interpretation techniques combining fracture datasets with
128 different resolutions to predict sub-seismic fractures?
- 129 b) What is the importance of integrating geometrical and topological attributes in the study
130 of fracture networks?
- 131 c) What is the complexity of natural fracture networks at sub-seismic scales?
- 132 d) Do fractures of distinct sizes observed at different scales present different attributes?

133 In summary, this work analyses the relationship between fracture sizes to test if there is
134 a correlation between their size and connectivity. It also aims to show a comprehensive
135 methodology to characterise fracture networks by the use of geometrical and topological
136 attributes of fractures at different scales of observation (outcrop, airborne LiDAR, seismic).

137 **2 Study areas and geological settings**

138 *2.1 Cariatiz carbonate platform, SE Spain*

139 At outcrop, the focus of this study is on the Messinian carbonate platform of Cariatiz,
140 which constitutes one of the pre-evaporitic Messinian sedimentary units in the Sorbas Basin
141 (Martín and Braga, 1994; Braga and Martín, 1996). The Cariatiz platform is located on the
142 northern margin of the Sorbas Basin, close to the village of Los Alías, SE Spain (Fig. 1). The
143 Sorbas Basin is oriented E-W and it is bordered by the Sierra de los Filabres to the north and
144 the Sierras Alhamilla and Cabrera to the south (Braga and Martín, 1996; Cuevas Castell et al.,
145 2007; Reolid et al., 2014; Nooitgedacht et al., 2018) (Fig. 1b). The formation of this Neogene

146 basin is linked to strike-slip (Jonk and Biermann, 2002) and extensional tectonism (Meijninger
147 and Vissers, 2006), comprising strata of Middle Miocene to Quaternary ages (Martín and
148 Braga, 1994; Reolid et al., 2014; Nooitgedacht et al., 2018). The geometry and stratigraphy of
149 the Cariatiz Fringing Reef Unit have been subject of extensive research (Riding et al., 1991;
150 Martín and Braga, 1994; Braga and Martín, 1996; Cuevas Castell et al., 2007; Sánchez-Almazo
151 et al., 2007; Reolid et al., 2014; Nooitgedacht et al., 2018).

152 The Cariatiz Fringing Reef Unit was chosen in this work because of its unique three-
153 dimensional exposure in which several fracture types with various sizes are recognised at
154 different scales (Fig. 4). During platform development, the Sorbas Basin was affected by a
155 regional tectonic uplift with a rate of *ca* 110 m/Myr, imposing a 3° dip to the Cariatiz platform.
156 Different reef growth phases appear as clinoform bodies (Reolid et al., 2014) which, in addition
157 to syn-depositional erosion, influenced the geometry of the platform (Cuevas Castell et al.,
158 2007). Sea-level changes have been reported as the governing mechanism controlling
159 carbonate productivity, reef slope geometry and stacking patterns of the clinoform bodies
160 (Kendall and Schlager, 1981; Braga and Martín, 1996; Reolid et al., 2014).

161 The Messinian Fringing Reef Unit comprises six distinct depositional facies (Riding et
162 al., 1991; Braga and Martín, 1996) (Fig. 4d). From the platform interior to the basin, these
163 depositional facies are as follows:

- 164 1. Lagoon – parallel beds of calcarenites and calcirudites with abundant gastropods, red
165 coralline algae, foraminifera, and mollusc remains. Small coral patches of *Porites* occur
166 near the reef crest. Siliciclastic grains are locally mixed with carbonate sediments.
167 Lagoonal beds dip 3° to the southwest (N216°E).
- 168 2. Reef framework – a 20 m thick unit subdivided into three sub-facies from top to bottom:

- 169 a. Reef crest zone (4-0 m water depth) – laminar to contorted *Porites* colonies with
170 stromatolitic crusts. Contains rudstones with echinoderms and molluscs fill
171 cavities.
- 172 b. Thicket zone (ca 4-10 m below the reef crest) – vertical corals and continuous
173 lateral coral growth.
- 174 c. Lower pinnacle zone (ca 10-15 m below the reef crest) – pinnacle morphologies
175 formed by columnar *Porites* connected by vertical and laminar coral growth
176 (Fig. 4e). Bioclastic matrix fills in remaining spaces.
- 177 3. Reef talus slope (uppermost slope) – deposits of reef framework blocks and coral
178 breccia with *Halimeda*, bivalves, molluscs, serpulids and coralline algae. Laminar
179 *Porites* colonies encrusting bioclasts are frequent.
- 180 4. Proximal slope (middle slope) – well-bedded deep water calcarenites and calcirudites
181 with bioclasts of serpulids, coralline algae, molluscs and abundant *Halimeda*.
- 182 5. Distal slope (lowermost slope) and basin – calcarenites, silty and sandy marls variably
183 intercalated with basinal marls and diatomites (upper part of the Abad Member).
- 184 6. Fan delta – episodic flows of fan delta sediments during carbonate platform growth,
185 alternating with conglomerates and sandstones intervals that interfinger with the
186 carbonate platform.

187 2.2 Pernambuco carbonate platform, East Brazil

188 At the seismic scale, our study focuses on the Pernambuco carbonate platform, which is
189 part of the eastern portion of the Brazilian continental platform, an area of stretched continental
190 crust forming the Pernambuco Plateau (Magalhães et al., 2014; Buarque et al., 2017) (Fig. 2).
191 The Pernambuco Basin is part of the Borborema Province, consisting of a complex collage of
192 continental masses (dos Santos et al., 2010; Buarque et al., 2017). This province was subject
193 of a series of Precambrian orogenic events, prior to late Mesozoic rifting stages that culminated

194 in continental breakup during the Cretaceous (Darros de Matos, 1999; dos Santos et al., 2010;
195 Buarque et al., 2017). The evolution of the basin was initially controlled by NE-SW and E-W
196 Precambrian shear zones that were then reactivated during rifting as strike-slip and normal
197 faults (Buarque et al., 2017). After that, the basin was controlled by NW-SE oblique transfer
198 faults, in addition to N-S, WNW-ESE and NNW-SSE normal faults, during the Aptian-Albian
199 (Buarque et al., 2017).

200 Buarque et al (2017) recognised five seismic sequences offshore Pernambuco. Seismic
201 Sequence 1 represents the beginning of a sag phase, comprising Aptian-Albian rift strata and a
202 salt layer. Salt layers generated large halokinetic features, such as diapirs and salt domes that
203 cross-cut Seismic Sequence 2, a unit composed of Cenomanian-Santonian post-rift strata
204 (Buarque et al., 2016, 2017, Fig. 7). Offshore carbonate deposition developed during two main
205 post-rift intervals: the Cretaceous post-rift Seismic Sequence 3 during the Campanian-
206 Maastrichtian, and the Lower Cenozoic post-rift Seismic Sequence 4 from Paleogene to Middle
207 Miocene. Upper Miocene to Recent strata occur in Seismic Sequence 5, described as an Upper
208 Cenozoic post-rift interval (Buarque et al., 2017 Figs. 4 and 5).

209 Sequences 3 and 4 comprise the Pernambuco carbonate platform (Fig. 2c). This platform
210 was chosen because of its distinctive km-long normal faults located along the platform margin
211 and platform interior, revealing a similar setting to the fractures observed on the platform
212 margin in Cariatiz, but at a larger scale (Fig. 2b and c). In addition, seismic characteristics
213 (geometries and seismic facies) observed in Pernambuco present similarities to the depositional
214 facies in Cariatiz (Fig. 2c). Four seismic facies are recognised in Pernambuco from the platform
215 interior to the basin:

- 216 1. Platform interior (lagoon) – semi-continuous to discontinuous, low- to medium-
217 amplitude internal reflections capped by a high-amplitude reflector.

- 218 2. Reef framework – semi-continuous sub parallel reflections bounded by the
219 platform margin, which coincides with a steep high-amplitude reflector.
220 3. Talus slope – chaotic, steep reflections with low- to medium- amplitude.
221 4. Slope and basin (including the proximal and distal slopes) – discontinuous,
222 chaotic reflections with low- to medium- amplitude.

223 **3 Methods and datasets**

224 Outcrop data from the Cariatiz carbonate platform are interpreted in this study, including
225 ten sampling sites and airborne LiDAR data covering an area of about 0.4 km² (Figs. 4, 5 and
226 6). Cariatiz is used as an outcrop analogue to understand the complexity of sub-seismic fracture
227 networks as the platform displays a multi-scale system of fractures identified from airborne
228 LiDAR maps down to the outcrop scale. The aim is to correlate fracture networks measured
229 from both field datasets to investigate the relationship between small and intermediate scale of
230 observations. In a later stage, a seismic dataset from the Pernambuco Basin in Brazil was used
231 to analyse fracture networks at a large scale. The methodology used in this work is summarised
232 in Fig. 3.

233 The main rationale behind the use of datasets from two different localities, and with
234 varied resolutions, was to investigate the effects of scale when characterising multi-scale
235 fracture networks. As observed from platform to basin transects of both platforms, seismic
236 facies and geometries from Pernambuco relate to depositional and structural settings at Cariatiz
237 (Figs. 2c and 4d). In addition, fractures are observed along the platform margin in both
238 Pernambuco and Cariatiz platforms (Figs. 2c and 4d). Nevertheless, each dataset has a
239 distinctive resolution in which a range of specific fracture sizes can be observed. Centimetre-
240 long fractures can be measured from exposure outcrop mapping, whereas fractures with a few
241 metres in length can be mapped from airborne LiDAR datasets, and kilometre fractures can be
242 measured utilising seismic data. This approach allowed us to understand which geological

243 features can be observed at each particular scale. Our analysis does not intend to suggest that
244 both platforms have the same fracture network properties, as they have different tectonic
245 histories. In fact, our results demonstrate the differences of fracture network properties
246 obtained from the two localities. However, the use of outcrop data can help to understand the
247 complexity of fracture networks at different scales of observation, and the amount of detail that
248 is lost due to data resolution.

249 *3.1 Topological sampling*

250 A fracture network is defined as a system of fractures developed within the same volume
251 of rock, and may include different fracture sets that could interact by connecting individual
252 fractures (Adler and Thovert, 1999; Sanderson and Nixon, 2015). An important part of our
253 workflow is to consider the topology of fracture networks from the three studied datasets.
254 Topology is the tool that allows geoscientists to properly characterise the connectivity (and
255 relationships) of a given fractured unit, in addition to geometrical attributes (Manzocchi, 2002;
256 Sanderson and Nixon, 2018). A combined analysis of fracture networks is the best practice, as
257 geometrical data on its own is not sufficient to produce a model reflecting the connectivity of
258 a fractured rock volume. In fact, two fracture networks with the same geometrical properties
259 (orientation, length) can show different connectivity (Sanderson and Nixon, 2018).

260 This work follows the models of Manzocchi (2002) and Sanderson and Nixon (2015) in
261 which fracture networks are considered in terms of traces (lines) and nodes (fracture
262 intersections and terminations) to form a system of branches between nodes (Fig. 7a). Fracture
263 network topology is given by the analysis of node types (I: isolated, Y: abutting or splaying,
264 X: crossing) and branch types (I-I: isolated, I-C: partly connected, CC: doubly connected). It
265 also involves resulting dimensionless parameters such as average number of connections per
266 line (C_L), average number of connections per branch (C_B), and dimensionless branch intensity
267 at percolation (B_{22C}) (Manzocchi, 2002; Sanderson and Nixon, 2015, 2018) (Figs. 3 and 7a,

268 Table D1). In order to further differentiate fracture populations, nodal functions such as the
269 N_B/N_L ratio, proportions of connecting nodes (isolated: P_I or connected: P_C) and branches
270 (isolated: P_{II} , singly connected: P_{IC} or doubly connected: P_{CC}) are useful to our analysis (Table
271 D1).

272 Topological data and resulting dimensionless parameters are analysed using a series of
273 equations and diagrams from Sanderson and Nixon (2015, 2018) (Table D1). A simple
274 approach to assess the topology and connectivity of fracture networks consists of plotting nodal
275 and branch data in ternary plots (Manzocchi, 2002; Sanderson and Nixon, 2015; Morley and
276 Nixon, 2016). Results from each dataset vary between outcrop locations, zones or depths. An
277 area covering the data variability is shown in ternary diagrams in addition to their average
278 values (Fig. 11). In this work, we used the Ternary Plot Maker (2019) to plot our data.

279 As suggested by Sanderson and Nixon (2015, 2018), dimensionless parameters such as
280 C_B , are useful measures to assess the connectivity of a fracture network. Values of C_B range
281 from 0-2. On a ternary diagram, low connected networks with C_B values close to 0, plot towards
282 the I-I corner, whereas high connected networks with C_B close to 2, plot towards the C-C corner
283 with a high proportion of interconnected branches. Furthermore, C_B can be used with B_{22C} to
284 estimate the percolation threshold of a given network topology. Sanderson and Nixon (2018)
285 demonstrated that most percolating systems have values of $C_B > 1.56$.

286 3.2 Geometrical sampling

287 Geometric parameters considered in this study are branch lengths and branch orientations
288 (strike), as they can be measured at different scales from the three provided datasets. Sanderson
289 and Nixon (2015, 2018) suggested that using branches instead of full traces is a better approach
290 to characterise fracture networks as it can avoid or decrease sampling errors (Fig. 7 b-f). These
291 errors can be related to (1) erroneous recognition, (2) censoring effects, and (3) truncation

292 effects (Manzocchi et al., 2009; Guerriero et al., 2010; Torabi and Berg, 2011 2011; Tao and
293 Alves, 2019).

294 Due to the complexity of fracture arrangements and the access limitation to entire fracture
295 networks (censoring), it is a challenging task to define the full fracture trace (Fig. 7b).
296 Erroneous recognition of the full fracture trace is common among interpreters as length and
297 orientation measurements of fracture traces may differ between different interpretations (Fig.
298 7b). Variations in the results (e.g. orientation and length) between interpreters can lead to
299 distinct and contrasting conclusions about a given fracture network. Identifying shorter
300 segments (branches) during interpretation is a consistent protocol to measure fracture
301 geometries (Fig. 7c). Results obtained utilising fracture branches can lead to similarities
302 between interpreters, avoiding the erroneous recognition bias, as the identification of the full
303 trace is not required.

304 Furthermore, censoring effects occur when a fracture extends beyond the sampling area
305 and the frequency of large fractures is underestimated (Fig. 7e). This effect can be reduced by
306 the use of fracture branches as the segment outside the sampling area is shorter (Fig. 7f). On
307 the other hand, truncation effects occur when small fracture frequencies are underestimated as
308 a result of resolution limitations that cannot be avoided due to data constraints (Fig. 7d).
309 Therefore, we stress the use of fracture branches in all measurements collected in this paper as
310 the obtained values can decrease uncertainties related to fracture sampling and provide more
311 reliable information about the geometrical parameters (length and orientation) (Fig. 7).

312 3.3 *Cariatiz Platform*

313 3.3.1 *Outcrop data – Field procedure*

314 Geometrical and topological attributes were measured from the Cariatiz reef framework
315 zone (Fig. 4a, d) on 10 outcrop surfaces (a 2D view of a fracture network) using the enhanced

316 circular scanline methodology of Watkins *et al.* (2015) (Fig. 5). More than 400 fracture traces
317 with ~1000 fracture branches were measured and analysed (Fig. 5). Topological analyses and
318 field procedures are similar to Sanderson and Nixon (2015) and Procter and Sanderson (2018)
319 in which we defined nodes and branches in the field and used rectified outcrop photographs
320 (Figs. 3, 5 and 7).

321 The first stage in our workflow was to select key sampling localities prior to fracture data
322 collection (Fig. 3). Sampling localities were initially chosen along the platform rim, within the
323 reef framework facies, using aerial photographs and LiDAR maps with elevation and slope
324 attributes (Fig. 6). This step was crucial to identify accessible areas where the fringing reef
325 could be mapped along exposed outcrop surfaces. Field measurements were dependent on how
326 clearly the fractures were exposed at the surface. Vegetation is preferentially localised within
327 fractures, as these are zones of intense weathering where soil accumulates and moisture is
328 retained, especially in arid conditions such as in Cariatiz (Boyer and McQueen, 1964; Aich and
329 Gross, 2008). As a result, soil and vegetation was present at some localities, indicating the
330 presence of open fractures (Fig. 5b, d). However, prior to fracture measurement, large
331 vegetation was removed, and soil was cleared from the outcrop surface.

332 The circular scanline sampling method was used to count the number of fracture
333 intersections at the edge of the circle (n) and the number of fracture terminations within the
334 circle (m) (Mauldon *et al.*, 2001; Watkins *et al.*, 2015) (Figs. 3 and 5). At each sampling
335 locality, a circle of known radius was drawn onto the surface using a length of rope with a stick
336 of chalk tied to the end (Figs. 3 and 5). The radius was chosen based on the minimum m and n
337 count (30) of Rohrbaugh *et al.* (2002) and Watkins *et al.* (2015) to ensure reliable fracture
338 estimates and identify individual fracture sets or data clusters (Fig. 3). Following the method
339 of Procter and Sanderson (2018), every node and branch was marked with chalk of different
340 colours, depending on their type, to help node and branch counting. A sketch of the fracture

341 network was drawn on the go to provide robust documentation of the measured data and to
342 guide digital interpretation at a later stage.

343 Once fracture nodes and branches were identified within the sampling circle, geometrical
344 measurements were performed in the field. The workflow included measuring fracture branch
345 orientation (strike, dip and dip direction), branch length, as well as identifying aperture and
346 fracture fill. By completion of topological and geometrical measurements, a photograph of the
347 locality was taken for a later use. Outcrop photographs of the circular scanline were rectified
348 using the graphics suite of CorelDraw and Corel PaintShop Pro in order to remove distortions
349 in 3D perspective (Fig. 5k, l). This process allows fracture attributes (branches, nodes) to be
350 digitised as a vector graphic image, in order to provide a clear representation to scale of the
351 outcrop fracture networks (Procter and Sanderson, 2018) (Fig. 5). Topological and geometrical
352 attributes were also measured digitally using the vector lineaments to confirm the values taken
353 in the field (Fig. 5). This process provides a good quality control of the measured data.
354 Additionally, vector lineaments allow accurate calculations of average orientations and exact
355 length measurements of irregular fracture branches. These latter measurements were the ones
356 used in the subsequent statistical analyses.

357 3.3.2 *LiDAR data – GIS analysis*

358 Airborne LiDAR imagery from the Cariatiz carbonate platform permitted the collection
359 of fracture measurements at an intermediate scale. Data was provided by the Instituto
360 Geográfico Nacional (IGN) and the Centro Nacional de Información (CNIG) of Spain (Fig. 6).
361 The airborne LiDAR map was acquired with a density of 0.5 points/m² with a 5 m grid size.
362 After processing for slope, a resolution of about 5 m is suggested for the airborne LiDAR
363 dataset. As a result, fractures of less than 5 m (below the LiDAR resolution) are subject to
364 truncation effects. Fracture branches ranging from a few metres to tens of metres in length can
365 be resolved from this dataset.

366 Visualisation and interpretation were carried out using ArcGIS 10.5. A slope attribute
367 was calculated from the LiDAR map to highlight intermediate-scale discontinuities (fractures
368 and fracture swarms) at Cariatiz (Fig. 6). A 3D visualisation of the LiDAR map, the slope
369 attribute map and aerial photographs were used simultaneously in our fracture interpretation to
370 be confident that the lineaments were real geological fractures and no other elements such as
371 footpaths or agriculture terraces related to abandoned olive fields (Fig. 6). The LIDAR map
372 was divided into three zones in order to understand spatial fracture variability in Cariatiz (Fig.
373 6b).

374 Each fracture branch was digitised as a single polyline to preserve geometrical
375 characteristics such as fracture branch length and orientation. Guidance from Nyberg et al
376 (2018) was used during the interpretation of fracture branches to avoid topological
377 inconsistencies such as erroneous short isolated fracture branches or overlapping fracture
378 branches. The snapping tool from GIS was crucial in this task. Node counting was performed
379 by digitising points at fracture terminations (I-nodes) or fracture intersections (Y-, X-nodes).
380 Geometrical attributes (length and orientation) were calculated using the “linear directional
381 mean” tool from the “spatial statistics tools” in ArcGIS.

382 3.4 Pernambuco carbonate platform

383 3.4.1 Seismic data

384 A post-stack depth-converted 3D seismic volume from the Pernambuco Plateau, offshore
385 East Brazil, was used in this study (Fig. 2). The seismic volume covers an area of 3,200 km²
386 with a vertical penetration of almost 9 km. The seismic volume was provided by CGG and
387 comprises 2700 inlines (IL) and 1899 crosslines (XL) with a 25 x 25 m line spacing and a
388 vertical sampling interval of 5 m. The interpreted seismic data is in depth domain with SEG’s
389 American polarity, and of good quality, allowing for the detailed analysis of fracture networks
390 on the wide platform margin (Fig. 8). There are no exploration wells in the study area.

391 Seismic attribute calculation and fracture interpretation were completed using
392 Schlumberger Petrel®. A variance cube was computed for the entire Pernambuco seismic
393 volume to compare the similarity of traces and highlight seismic discontinuities such as faults
394 and fractures (Chopra and Marfurt, 2007; Brown, 2011; Marfurt and Alves, 2015) (Figs. 3 and
395 8). Eleven depth slices were analysed and interpreted from $Z = -1020$ to -2020 m at intervals of
396 100 m (Figs. 3 and 8). Fault interpretation was performed on a portion of the Pernambuco
397 carbonate platform covering the shelf and slope. Faults were interpreted by visualising depth
398 slices and seismic sections simultaneously to make sure that lineaments are real faults with a
399 vertical displacement and avoid interpretation of artefacts (Fig. 2c). Data was then exported to
400 Esri® ArcGIS Desktop where geometrical (branch length, orientation) and topological (nodal
401 and branch counting) analyses were performed using the same methodology as with LiDAR
402 data (Figs. 3 and 8).

403 3.5 *Statistics and data analyses*

404 A common practice to analyse geometrical attributes of a fracture network is to use rose
405 diagrams and frequency distribution plots such as histograms and cumulative plots (Watterson
406 et al., 1996; Odling, 1997; Nyberg et al., 2018). The geometrical data in this work is analysed
407 by equal area rose diagrams and branch length-frequency plots. Branch length measurements
408 were processed using Microsoft Excel, where histograms, box plots, a series of cumulative
409 frequency plots, and tables with statistical data were compiled in order to identify distribution
410 trends (negative exponential, log-normal or power law) in a similar way to Nyberg et al. (2018)
411 (Fig. 9).

412 Fracture orientation measurements were processed using the Matlab® version of MARD
413 1.0 by Munro and Blenkinsop (2012). Rose diagrams were plotted using a bi-directional
414 function with a weighted moving average and equal area. The weighting factor for all plots was

415 0.9 with a 9° aperture angle for data averaging (Figs. 10 a-c, B1 and B2). Visual analyses from
416 these rose diagrams suggest that our data is multimodal with different fracture sets (Fig. 10).

417 Numerical techniques were key in our workflow to define specific fracture sets.
418 Multimodal orientation datasets were divided into clusters utilising the cluster analysis tool in
419 Orient 3.11.1 (Vollmer, 1990, 1995, 2015) (Fig. 10 d-f). The cluster analysis method included
420 axial data in which the number of clusters (from 2 to 9) is defined by the user. Every data
421 sample was tested using different number of clusters in which the dominant sets were mostly
422 defined regardless of the cluster counts. Visual interpretation of fracture sets based on equal
423 area rose diagrams (Fig. 10 a-c) was useful in determining the final selection of the number of
424 clusters (Fig. 10 a-c). For every fracture set, the axial mean was calculated using the Statistics
425 Tool within Orient 3.11.1.

426 **4 Results – Fracture network characterisation**

427 *4.1 Fracture complexity*

428 In this study, we recognised different fracture types depending on the scale of
429 observation. At outcrop scale, fracture compartmentalisation, chaotic and curved stylolite
430 surfaces, as well as vertical *Porites* on the platform edge, show how complex the structural and
431 depositional attributes are on carbonate platforms like Cariatiz (Figs. 4 and 5). Open fractures
432 (joints) and veins were recognised across the Cariatiz Reef Unit (Figs. 4 and 5g, h). Veins have
433 calcite infill and can be observed in many of the circular scanlines analysed (Fig. 5g). Large
434 vertical fractures are visible across the reef framework zone, extending from the reef crest down
435 to the slope facies zone (Fig. 4a). These fractures create blocks and are related to slope
436 instability.

437 From airborne LiDAR imagery, the main structures comprise fracture swarms composed
438 of clusters with closely spaced fractures. These fracture swarms are identified in the field (Fig.

439 4c) but can be better mapped and measured with slope attribute maps from airborne LiDAR
440 data (Fig. 6). At the largest (seismic) scale of Pernambuco, normal faults are observed from
441 different depth slices and profile sections (Fig. 8). These faults have variable throws ranging
442 from a few tens of metres (reaching the data resolution) up to 300 m in some areas (Fig. 2c).
443 These faults have regional and large-scale tectonic origins in contrast to those observed at
444 outcrop.

445 4.2 Fracture network geometry

446 4.2.1 Fracture length

447 4.2.1.1 Cariatiz platform – Outcrop data

448 The length of fracture branches at Cariatiz displays a wide range of sizes (Figs. 9a, b and
449 A1). However, every site has a similar distribution of fracture branch lengths with a positive
450 skew (Fig. A1). Data gathered from the ten field sites also have a positive skew, showing that
451 smaller fracture branches are the most abundant with centimetre lengths (Figs. 9a and A1).
452 Higher frequencies are observed in fractures ranging from 9.4 cm to 33.8 cm with a medium
453 value of 19.3 cm and a mean of 25 cm (Fig. 9b).

454 Sites A and C present a unimodal distribution with a positive skew. The dominant lengths
455 are 3 to 25 cm (Fig. A1a, c). Fracture branch length at Sites B and I show a multimodal
456 distribution (Fig. A1b, i). There are two dominant peaks with ranges of 3 to 13 cm and 31 to
457 41 cm (Fig. A1b, i). Sites D and G have a bimodal distribution with major fracture length
458 frequencies ranging from 5 to 17 cm and 21 to 39 cm in length (Fig. A1d, g). Fracture
459 distribution in Site E shows a large positive skew with the highest frequency observed in
460 fractures ranging from 3 to 11 cm (Fig. A1e). Sites F and H present a major peak in fractures
461 ranging from 9 to 21 cm in length (Fig. A1f, h). Site J has a positive skew distribution, with a
462 highest peak representing fractures from 3 to 21 cm in length (Fig. A1j).

463 We plotted cumulative percentages of fracture branch lengths to determine if they fit a
464 distribution trend such as negative exponential, log-normal or power-law distribution models
465 (Figs. 9c, d, e). Outcrop data is best represented by a negative exponential or lognormal
466 distribution (Fig. 9d). A deviation from this trend is observed for the longest branches due to
467 truncation effects.

468 4.2.1.2 *Cariatiz platform – LiDAR data*

469 Airborne LiDAR imagery has a resolution of 5 m, implying that lineaments with sizes
470 below this value, such as centimetre-long fracture branches mapped at outcrop (joints and
471 veins), cannot be identified on the LiDAR map (Fig. 6). Instead, fracture swarms that are
472 difficult to measure at outcrop (Fig. 4c), can be easily recognised and measured at this scale
473 (Fig. 6). Areas that appear to be highly fractured at outcrop, such as Site C (Fig. 5c), appear as
474 areas with no fractures on the LiDAR map (Fig. 6), a character related to the absence of fracture
475 swarms in that section of the platform.

476 The study area was divided into three different zones in order to understand fracture
477 variability along the platform margin (Fig. 6b). Fracture branch length at the LiDAR scale
478 ranges from 1.4 to 47 m. Data present a positively skewed distribution, similar to outcrop data
479 (Fig. 9f, g). The higher concentration of fracture branches is observed from 5 m to 11.8 m, with
480 a median value of 7.4 m and a mean of 9.2 m (Fig. 9f, g). Zones 1 and 3 have a positively
481 skewed histogram (Fig. A1k, m). The dominant fracture branch length ranges from 4 to 11 m.
482 Zone 2 has more variability with a less positive skewed histogram and dominant fracture
483 branch lengths ranging from 6 to 20 m (Fig. A1l).

484 Plots of cumulative percentage against fracture branch lengths display a similar pattern
485 to the outcrop data, having the best fit with a negative exponential or log-normal distribution

486 (Figs. 9h, i, j). A power-law distribution is only representative with fracture branches longer
487 than 10 m.

488 4.2.1.3 Pernambuco platform – Seismic data

489 Fractures (faults) in the range of hundreds of metres to a few kilometres predominate on
490 seismic data from Pernambuco. These faults have throws ranging from a few metres up to 300
491 m (Fig. 2c). In Pernambuco, the highest fracture frequency is represented by features between
492 636 m to 1360 m with a median value of 926 m, and a mean of 1064 m (Fig. 9k, l). Due to its
493 resolution, features that were observed in the field at the Cariatiz platform such as fracture
494 swarms, joints and veins are not visible in seismic data.

495 Fracture branch length distribution from depth slices at $Z=-1020$ m and $Z=-1220$ show a
496 positive unimodal skew. The major peak is observed with branch lengths of 300 to 700 m (Fig.
497 A2a, c). At a depth of -1120 m, fracture branch lengths have a multimodal distribution with a
498 concentration of fractures between 500 to 600 m. Fault lengths range from 200 m to 2500 m
499 (Fig. A2b).

500 The variance slice at a depth of $Z= -1320$ m shows a multimodal distribution with length
501 peaks at 700 m, 1100 m, 1400 m and 1700 m. Most of the data ranges from 200 m to 2600 m
502 with a few outliers (Fig. A2d). At $Z= -1420$ m, a slight positive skew with unimodal distribution
503 is observed (Fig. A2e). The dominant fracture branch length ranges from 600 m to 1200 m
504 (Fig. A2e). Fracture branch length distribution at $Z= -1520$ m ranges from 300 m to 3100 m,
505 with predominant fractures between 700 m to 1100 m (Fig. A2f). A unimodal distribution is
506 recognised on the variance slices at $Z= -1620$ m, -1720 m, -1820 m, -1920 m and -2020 m.
507 Fracture branch lengths range from 300 m to 3500 m. At these depths, the dominant values
508 range from 500 m to 1300 m. A positive skew with a long tail towards the larger values is
509 observed in all histograms (Fig. A2g, h, i, j, k). A negative exponential or log-normal

510 distribution plot displays a reasonable fit over most of the data range at seismic scale. A poor
511 fit is observed in longer faults (Fig. 9m, n, o).

512 4.2.2 Fracture orientation

513 4.2.2.1 Cariatiz platform – Outcrop data

514 Fracture strike distributions from field measurements differ slightly from site to site with
515 rose diagrams showing different orientations at each locality (Figs. 1c and B1). Data gathered
516 from all localities display a multimodal distribution with fractures striking nearly in all
517 directions with similar frequencies (Fig. 10a). However, four fracture sets are defined based on
518 the cluster analysis (Fig. 10d). The first two sets strike NE and E-W with an axial mean of
519 N51°E and S89°E, respectively. The third set strikes SE (S38°E) followed by a fourth set
520 striking N-S (S11°W). The axial mean of fracture set 1 is almost parallel to the orientation of
521 the Cariatiz platform margin (Fig. 10d).

522 Sites A and B contain fracture sets with a multimodal distribution (Figs. 1c and B1a, b).
523 Three fracture sets with high frequency are recognised. The first one strikes NE, while the
524 second and third sets strike NW. Site C and D exhibit three fracture sets; the highest frequency
525 coincides with a SW strike, followed by E-W fractures and a set striking to the SSW (Figs. 1c
526 and B1c, d). Outcrop surfaces at Sites E, F and G exhibit two main fracture sets: a first set with
527 a NW strike, and a second set striking widely NE (Figs. 1c and B1e, f, g). Fractures at Site H
528 exhibit three main fracture sets, with the most dominant striking NE. The second and third
529 fracture sets strike to the WNW and to the NW (Figs. 1c and B1h). Fractures at Sites I and J
530 show a dominant NE strike, followed by a NW strike (Figs. 1c and B1i, j).

531 4.2.2.2 Cariatiz platform – LiDAR data

532 The average orientation of the Cariatiz carbonate platform margin is N55°E, as observed
533 from the aerial and LiDAR maps (Figs. 6 and 10b). Three fracture sets are recognised on

534 LiDAR data along the Cariatiz fringing reef (Fig. 10e). The dominant Set 1, with the highest
535 frequency, strikes to the NE (N59°E), in a direction similar to the edge of the platform margin
536 (Figs. 6, 10b and e, and B1k, l, m). The second and third minor fracture sets strike to the N-S
537 (N02°W) and SE (S71°E), respectively. The second fracture set is recognised in the three zones,
538 but it is more predominant in Zone 1 (Fig. B1k).

539 4.2.2.3 Pernambuco platform – Seismic data

540 The orientation of the Pernambuco carbonate platform margin is N50°E as observed from
541 seismic depth slices (Figs. 2b and 10c). Cluster analysis of fault orientation data from the eleven
542 depth slices reveal a major set of faults (Set 1) aligned NE (N48°E), a direction parallel to the
543 platform edge (Fig. 10 c and f). Two minor fracture sets with lower frequencies, striking N-S
544 and E-W, are also recognised with axial means of S09°E and S77°E, respectively (Fig. 10f).

545 From each depth of observation, data can be summarised as follows. Fractures at Z=-
546 1020 m depth predominantly strike NW (Fig. B2b). Two secondary sets are also recognised
547 with NE and NNW strikes. At depths of Z= -1120 m, -1220 m, -1320 m and -1420 m, there are
548 similar fracture orientations with a dominant set striking to the NE, followed by two minor
549 fracture sets striking NNW and WNW (Fig. B2c, d, e). A primary fracture set striking NE is
550 recognised from Z= -1520 m to -2020 m (Fig. B2g, h, i, j, k, l).

551 4.3 Fracture network topology

552 4.3.1 Cariatiz platform – Outcrop data

553 Abutting or Y nodes are the dominant type of nodes at the outcropping Cariatiz platform.
554 Nodal data change slightly at each locality, which is observed as a zone of variability on the
555 ternary plots (Figs. 11a, C1a). Based on our average results, the proportion of isolated nodes
556 (P_I) at outcrop is low with a value approaching 9%, whereas the proportion of connected nodes
557 (P_C) is 91% (Table D2). At Cariatiz, from outcrop scale, branch classification shows that

558 isolated branches (P_{II}) are only 0.8%. The highest proportions are related to connected branches
559 with 8.3% being singly connected (P_{IC}) and 82.4% being doubly connected (P_{CC}) (Table D2).
560 The N_B/N_L ratio ranges between 2 to 4, but most values lie around 3, suggesting that small
561 scale-length fracture networks are dominated by abutting or splaying fracture terminations
562 (Figs. 11b, C1b, Table D2).

563 From the connectivity analysis we determined that in Cariatiz, the average number of
564 connections per line (C_L) ranges from 2 to 5, with 50% of the data ranging between 3 to 4 (Figs.
565 11c, C1c, Table D2). Moreover, 70% of the outcrop fractures at Cariatiz have a C_B value
566 ranging between 1.8 to 2 (Figs. 11d, C1d, Table D2), suggesting that the fracture network is
567 well connected, mostly by Y nodes. High values of C_B also indicate that fracture networks at
568 Cariatiz are above the percolation threshold. The branch classification diagram plots values
569 towards the C-C corner (Figs. 11e, C1e), stressing the high proportion of interconnected
570 branches at Cariatiz, which can favour fluid flow.

571 Fracture networks from localities B, C and I are less connected than most data and are
572 typical of multimodal joint networks (see Procter and Sanderson, 2018) (Fig. C1a). These
573 localities have tree-like geometries based on the average degree $\langle d \rangle$ value from Sanderson et
574 al (2019).

575 4.3.2 *Cariatiz platform – LiDAR data*

576 LiDAR data indicates that on average, 51% of the nodes are of type I and 47% are of
577 type Y, with only 2% of X nodes (Figs. 11a, Table D2). It suggests that fracture connectivity
578 at a metre-scale is not as developed as at the centimetre-scale. At an intermediate scale, the
579 proportion of isolated nodes (P_I) is 25%, and connected nodes (P_C) is 75% (Table D2). Branch
580 classification reveals that proportions of isolated branches (P_{II}) represent 6.5% of the network

581 and singly connected branches (P_{IC}) comprise 19% of the network. Higher proportions relate
582 to doubly connected branches (P_{CC}) with 55.5% (Table D2).

583 The N_B/N_L ratio has a value of 2, suggesting low proportions of connected branches at
584 the metre-scale (Fig. 11b, Table D2). The average number of connections per line (C_L) and per
585 branch (C_B) are also lower than at outcrop, with values of 2 and 1.5, respectively (Fig. 11c, d,
586 Table D2). Despite the observed low values of branch connectivity, single and double
587 connected branches dominate the fracture network at the metre scale (Fig. 11e, Table D2).
588 These fracture networks are tree-like and multicomponent, which suggest that the fractures
589 observed here are localised and therefore not part of a connected regional system (Sanderson
590 et al., 2019).

591 4.3.3 Pernambuco platform – Seismic data

592 Fracture topology on the Pernambuco carbonate platform is represented on average, by
593 39% of I nodes, 54% of Y nodes and 7% of X nodes (Figs. 11a, C1g, Table D2). The average
594 proportions of having isolated nodes (P_I) is 17%, and the proportion of connected nodes (P_C)
595 is 83% (Table D2). These proportions are similar to Cariatiz, as the proportions of connected
596 nodes are higher than isolated nodes (Table D2). Regarding proportions of branches in
597 Pernambuco, the proportion of isolated branches (P_{II}) are 2.9% (P_{II}) followed by singly
598 connected branches (P_{IC}) with 14%. Higher proportions are observed in doubly connected
599 branches (P_{CC}) with 69.1% (Table D2).

600 The N_B/N_L ratio ranges from 2 to 3 (Fig. 11b, C1h, Table D2). The average number of
601 connections per line (C_L) is 2.64, with a range between 2 and 3. The average number of
602 connections per branch (C_B) has a wider range from 1.4 to 1.8 and a median value of 1.66,
603 suggesting a moderate fracture connectivity at the seismic scale and networks close to the
604 percolation threshold ($C_B = 1.56$) (Sanderson and Nixon, 2018) (Fig. 11c, d; C1j, l; Table D2).

605 Doubly connected branches dominate the fracture network at seismic scale (Fig. 11e, C1k,
606 Table D2).

607 **5 Discussion**

608 *5.1 Fracture attribute relationships at different scales*

609 Previous studies have explored the idea of limitations due to data resolution and the
610 effects of scale on the spatial arrangements of fault and fracture networks. For instance, studies
611 such as Strijker et al. (2012) and Gutmanis et al. (2018) have examined the challenges of
612 analysing sub-seismic fracture networks and the presence of an “intermediate” data gap
613 between fractures observed from seismic and borehole datasets. Furthermore, extensive
614 research including Odling (1997) and Watterson et al. (1996) have discussed scaling
615 relationships of fracture networks and the uncertainties related to sampling effects. Pickering
616 et al. (1997) and Nixon et al. (2012) have also suggested that resolution limitations of seismic
617 data affect the estimation of fault network parameters such as connectivity, as this appears to
618 change depending on the data resolution.

619 This paper aims to perform a multi-scale analysis to understand the inherent complexity
620 of natural fracture networks, the existing differences at each scale and their scale dependency.
621 A way to understand sub-seismic features is by using outcrop analogues. For this reason, we
622 utilised exposure mapping and airborne LiDAR maps from the Cariatiz carbonate platform in
623 SE Spain. In parallel, seismic datasets such as the one from the Pernambuco carbonate platform
624 in Brazil are important to study km-long subsurface features. It is recognised from geometrical
625 and topological analyses of fracture networks from Cariatiz that they have different attributes
626 depending on the scale of observation, which may also be related to the distinct fracture types
627 observed at each scale (Fig. 12).

628 5.1.1 Fracture geometry

629 5.1.1.1 Orientation

630 The Cariatiz carbonate platform margin is oriented N55°E (Fig. 10). Fracture branch
631 orientation data differ between centimetre scale-length (outcrop) and metre scale-length
632 (LiDAR) fractures. Rose diagrams from each dataset have different distributions, implying that
633 fracture development may vary depending on scale (Fig. 10). Equal area rose diagrams
634 demonstrate a multimodal distribution of fracture orientations at outcrop (Fig. 10 a and d).
635 These fractures are specifically recognised as open joints and calcite filled veins (Figs. 5g, h
636 and 12a). Numerical methods of cluster analysis helped us to divide the data into four fracture
637 sets with similar frequencies (Fig. 10d). Fracture set 1 is important as it strikes parallel to the
638 Cariatiz platform margin with an axial mean of N51°E (Fig. 10d).

639 At airborne LiDAR scale, the main lineaments comprise large fracture swarms that may
640 be better related to gravitational instability at the edge of the platform margin (Figs. 4c, 6 and
641 12a). Small centimetre-length fractures identified from the outcrop exposure mapping are not
642 visible at LiDAR scale due to limitations in resolution, as the smallest features identified are
643 about 5 m in length (Figs. 6 and 9g). Furthermore, the orientation distribution and cluster
644 analysis of fractures observed from airborne LiDAR data show a clear dominant fracture set
645 striking NE-SW, with an axial mean of N59°E (Fig. 10e). The orientation of the Cariatiz
646 platform margin (N55°E) is similar to the dominant fracture set 1 identified from LiDAR data
647 (Fig. 10e), suggesting that intermediate scale-length fractures are dependent on the geometry
648 of the platform (Figs. 6 and 10e).

649 The orientation of the Pernambuco platform margin is N50°E (Fig. 10f). Similarly to
650 LiDAR data from the Cariatiz platform, the dominant fracture set recognised from the equal
651 area rose diagrams and cluster analysis, is parallel to the platform margin with an axial mean
652 of N48°E (Fig. 10c and f). This result suggests that fractures at intermediate and large scales,

653 namely fracture swarms and kilometre faults respectively, are mainly controlled by the
654 geometry of the platform margin (Figs. 8 and 10). Although there is a fracture set recognised
655 at outcrop that also correlates to the Cariatiz platform margin, it is not the most dominant set
656 at the cm scale. This suggests that at outcrop, fracture development is also highly controlled by
657 other processes such as intense weathering, and the uplift of the platform, in addition to
658 gravitational instability at the proximity of the platform edge.

659 5.1.1.2 Scale gap

660 Studies such as Strijker *et al.* (2012) have identified a scale gap between fractures
661 resolved on seismic and borehole data. Outcrop data from this study are used to describe
662 fractures that occur in this “intermediate” gap. Scale gaps are created by the limited resolution
663 of the imaging methods, and resolution is given by the smallest feature that can be observed
664 and measured in a specific dataset. We recognise that exposure mapping from outcrop data can
665 be useful to identify joints and veins (Fig. 5g, h) covering three orders of magnitude with
666 fracture branches ranging from 10^{-3} to 10^0 m in length (Fig. 12a). Airborne LiDAR data can
667 cover two orders of magnitude with fracture branches ranging from 10^0 to 10^2 m in length (Fig.
668 12a), with the main observed features being fracture swarms. Fracture branch length
669 measurements from outcrop and LiDAR data at Cariatiz, show that the higher frequencies of
670 branch lengths range from 10 to 34 cm and 5 to 12 m, respectively (Figs. 9b, g and 12).

671 Fracture lengths in both datasets are below seismic resolution. Even the less abundant
672 and largest fracture branches recognised on LiDAR, which are part of the outliers of the data,
673 have lengths of less than 50 m. Given a line spacing of 25 x 25 m on a seismic dataset, these
674 fracture lengths would be subject to truncation effects and not visible from seismic data (Figs.
675 9g, d and 12). Moreover, the smallest fracture branch length recognised on seismic data is 100
676 m (Figs. 9k, l and 12). As a result, a scale gap in terms of fracture branch length is observed
677 with no overlap between datasets (outcrop-LiDAR and LiDAR-seismic) due to the fact that

678 resolution limits in the imaging methods constrain reliable fracture characterisation (Fig. 12a).
679 A fundamental issue when measuring fractures from any source of data is the inherited
680 limitation of the sampling bias due to censoring and truncation effects (Guerriero et al., 2010;
681 Torabi and Berg, 2011 2011) (Fig. 7). These effects can cause under- or over- estimation of
682 statistical parameters, compromising the results of fracture characterisation.

683 As observed in the field, fractures at the “transitional” scale do exist in nature, and the
684 gap can be breached by the use of a dataset that can cover the resolution of those features. For
685 instance, large vertical fractures are observed at the edge of the Cariatiz platform, creating
686 compartmentalised blocks (Fig. 4a). Those fractures have high censoring effects at the outcrop
687 scale as they extend outside the observable area, and at airborne LiDAR they are not identified
688 due to truncation effects; therefore their presence is underestimated (Figs. 7d, e and 12a).

689 The Pernambuco seismic data is useful to understand features (faults) that one can
690 encounter when analysing large carbonate platforms such as Pernambuco’s, which is more than
691 40 km wide and hundreds of kilometres long (Fig. 2). From our analysis we determined that at
692 this scale, fracture branches can be observed and measured with a range of 10^2 to 10^4 m in
693 length (Fig. 12a). However, when comparing large carbonate platforms with smaller structures
694 such as isolated carbonate platforms (ICPs), these latter have dimensions ranging from 2 to 18
695 km, such as those ICPs in the North West Shelf of Australia (Loza Espejel et al., 2019) and the
696 South China Sea (Zampetti et al., 2004, Fig. 15). Internal fault branches within these structures
697 are a few hundreds of metres long and cannot be fully resolved in seismic data. These types of
698 faults would be part of the “transitional” gap that cannot be resolved by the use of datasets with
699 comparable scales to either airborne LiDAR maps or seismic data (Fig. 12a). Only large,
700 regional faults crossing the ICPs can be easily observed in seismic data. This is related to the
701 size of the fractures as well as the seismic response in ICP facies. ICP facies are typically
702 characterised by chaotic and low amplitude reflectors (Burgess et al., 2013; Loza Espejel et al.,

703 2019). Any feature below this range is considered as sub-seismic and therefore additional data
704 with higher resolution is required to be able to observe these faults (Fig. 12a).

705 The problem of scale gaps between datasets is partly related to the fact that, in all datasets,
706 the highest frequency of fracture branch lengths is concentrated at the smaller lengths of each
707 resolution, which is observed from histograms in the form of a positive skew distribution (Figs.
708 9). Even if there is a small overlap and fractures of similar length can be observed from two
709 different scales of observation, those measurements are on the limit of the resolution of both
710 datasets and therefore not representative due to censoring and truncation effects. The gap size
711 will depend on the detail and parameters of the data acquisition for different datasets.

712 In order to obtain a better controlled model of the fracture network characterisation, it is
713 critical to bridge those gaps and obtain datasets in which fracture observations considerably
714 overlap from one dataset to another. This can be done by acquiring datasets with higher
715 resolutions. For instance, to link outcrop observations with aerial LiDAR maps, high-resolution
716 drone imagery or ground-based LiDAR mapping could be used (Fig. 12a). To link LiDAR and
717 seismic datasets, changes to acquisition parameters of LiDAR maps and seismic volumes could
718 be made to increase the data resolution; or if possible, an intermediate-scale high resolution
719 seismic survey could be acquired to bridge the scale gap between the seismic and airborne
720 LiDAR data (Fig. 12a). This is important, as higher resolution seismic data processed to image
721 a certain depth (and frequency spectrum) can reveal fracture patterns that the original
722 exploration surveys may not have imaged in the first place, as the original interest was to image
723 the entire thickness of sediments on a basin.

724 5.1.1.3 *Branch length*

725 There has been much discussion on whether fracture trace length distributions are
726 exponential or power-law (Needham et al., 1996; Nicol et al., 1996; Gillespie et al., 2001; Zeeb

727 et al., 2013; Liu et al., 2016). Studies such as Gillespie *et al.* (2001) and Strijker *et al.* (2012)
728 have analysed fracture trace length distributions from different datasets and concluded that for
729 massive, non-stratabound units, fracture trace lengths can be represented by a power-law
730 distribution, while stratabound units can be represented by a lognormal distribution. Despite
731 the wide range of published work on trace length distribution, there seems to be a lack of
732 knowledge in the literature about branch length distributions.

733 The Cariatiz platform has a complex geometry in which bedding cannot be observed at
734 the reef framework; instead, massive rock units are intensely fractured to create large blocks
735 and compartmentalise the carbonate unit (Fig. 4). Branch length analysis from outcrop and
736 LiDAR data suggest that, for massive units like Cariatiz, a negative exponential distribution
737 better represents the fracture distribution, with a deviation for longer trace lengths due to
738 truncation effects (Fig. 12c). Such a trend can be expected to extend over longer fracture
739 branches, as fracture distribution in Pernambuco with km-long fractures follows the same trend
740 (negative exponential or log-normal distribution; see cumulative plot in Fig. 9n). This may
741 suggest that, in order to predict smaller scale-length fracture branches when utilising seismic
742 data, a negative exponential distribution can be used. This is of particular importance to
743 reservoir characterisation in which prediction of sub-seismic fractures is key.

744 5.1.2 *Fracture topology*

745 Topology is a relevant aspect when characterising fracture networks as dimensionless
746 parameters can be obtained to understand specific attributes such as connectivity (Sanderson,
747 2016; Sanderson and Nixon, 2018). Exposed outcrops on the Cariatiz carbonate platform
748 allowed a detailed analysis of fracture network distribution (Fig. 11). Outcrop results show a
749 variability cloud with an average of high proportions of connected nodes (mostly Y) and low
750 proportions of isolated nodes. Conversely airborne LiDAR results demonstrate that larger
751 fracture branches at Cariatiz have less connected nodes with an almost equal proportion of I

752 and Y nodes (Figs. 11a, C1a and Table D2). The average number of connections per branch
753 analysis (C_B) demonstrates that outcrop data are better connected than LiDAR data with an
754 average of 1.8 and 1.5, respectively (Figs. 11d, C1d and Table D2).

755 Branch classification shows that outcrop scale fractures have high proportions of doubly
756 connected branches and low proportions of singly connected branches with almost no isolated
757 branches. LiDAR data is also dominated by doubly connected branches, but with lower
758 proportions than the observed at outcrop as isolated branches have slightly higher proportions
759 (Figs. 11e, C1e and Table D2). Branch classification thus suggests that smaller fractures have
760 a higher probability to form connected branches (single and double) than larger fractures
761 observed on the LiDAR map. This can be confirmed by the analysis of connections per branch
762 and dimensionless intensity (Manzocchi, 2002; Sanderson and Nixon, 2018).

763 Sanderson and Nixon (2018) suggested that dimensionless parameters such as the
764 average of connections per branch (C_B) and dimensionless branch intensity (B_{22C}) are useful
765 measures of connectivity. These measures are also related to percolation in which systems with
766 $C_B > 1.56$ can indicate percolation. Topological results from Cariatiz were plotted using Fig.
767 10d from Sanderson and Nixon (2018) (Fig. 11f). From this diagram it is observed that fractures
768 at outcrop are mostly plotted above the percolation threshold, whereas fractures from the
769 LiDAR data plot just below the percolation threshold. When comparing the higher values of
770 C_B for outcrop data ($C_B=1.8$) with those obtained by LiDAR ($C_B=1.5$), the results suggest that
771 small length scale fractures are better connected than intermediate length fractures (Fig. 11f).
772 These results align with the observations from Nixon et al (2012, Fig. 14), suggesting that for
773 carbonate platforms comparable to Cariatiz, fracture connectivity increases with increasing
774 data resolution. Fault networks appear to be less connected at lower resolutions according to
775 the latter authors.

776 If the connectivity trend recognised from outcrop and LiDAR continues towards larger
777 fracture lengths, in a similar way to the trend observed by Nixon et al (2012, Fig. 14) as a
778 function of data resolution, longer faults and fractures at Cariatiz, resolvable at seismic scale,
779 would be expected to plot closer to the I node corner (Fig. 11d). These topological values
780 expected at seismic scale would have lower values of C_B and therefore be less connected (Fig.
781 11d). This observation is important as it suggests that topological results at the largest scale
782 analysed (e.g. seismic), are expected to have lower values of connectivity than fractures
783 analysed at small scale (e.g. outcrop), given that connectivity may increase as the resolution
784 increases and smaller fracture branches are measured. This trend is expected to occur in
785 carbonate platforms with similar settings to Cariatiz, in which connectivity decreases as scale
786 is increased. Further research is however needed in order to accurately predict the exact range
787 of topological values at a different scale.

788 At seismic scale in Pernambuco the average proportions of connected nodes are
789 considerably higher than the proportions of isolated nodes. Doubly connected branches have
790 also higher proportions than singly connected and isolated branches. In Pernambuco, the
791 average number of connections per branch (C_B) is 1.66 (Table D2) and, when analysed together
792 with the dimensionless branch intensity at percolation (B_{22c}), it is observed that the values are
793 on average, well connected and above the percolation threshold (Fig. 11i). As stated from the
794 Cariatiz topological trend, topological results of large fracture branches from the Pernambuco
795 carbonate platform analysed from seismic scale (large scale) are expected to have lower
796 connectivity values than sub-seismic smaller fractures. Consequently, sub-seismic fractures in
797 Pernambuco are expected to be better connected with values plotted closer to the Y node corner
798 and higher values of C_B (Fig. 11j).

799 5.2 *Implications to naturally fractured reservoirs*

800 Fracture network characterisation plays an important role in hydrocarbon exploration and
801 the development of naturally fractured reservoirs. It is known that the use of outcrop analogues
802 is key to predict sub-seismic fracture networks, particularly when borehole data (e.g. well
803 cores, image logs) are not available and there is the need to estimate the volume capacity and
804 fluid flow of a given unit (Gutmanis et al., 2018). Outcrop analogues can provide valuable
805 information on the behaviour of small (centimetre) and intermediate (metre) scale fracture
806 networks by the combination of outcrop and LiDAR data, respectively. Predicting the geometry
807 (orientation and length) and topology (dimensionless parameters) of fracture networks at sub-
808 seismic scales is crucial to increase the quality of fracture network characterisation. The study
809 from Cariatiz demonstrates that fracture networks at a smaller scale (e.g. outcrop) have a higher
810 level of connectivity than in a larger scale (e.g. LiDAR) with higher values of C_B . We may
811 predict that sub-seismic fractures have a better connectivity than seismic fractures. Topological
812 parameters measured from seismic data represent lower values of connectivity compared to
813 smaller fractures expected within the reservoir. Fracture network results obtained from
814 fractures observed at seismic (km long) scale are not representative for the multi-scale fracture
815 system, and only describe the parameters of km-long fracture branches. As a result, fracture
816 reservoir models utilising topological parameters obtained from seismic fractures (km-long)
817 may underestimate the presence of fractures at lower scales of observation. Areas that appear
818 to have no faults on seismic data, might be highly fractured as observed in Cariatiz (Figs. 5 and
819 6). Consequently, a potential reservoir could be ignored if proper studies are not performed. To
820 fully characterise the fracture system at different scales, including the reservoir, topological
821 and geometrical analyses like those presented for Cariatiz and Pernambuco should be
822 performed. Furthermore, negative exponential or log-normal distribution trends can be used to

823 predict sub-seismic fracture branch lengths. It is advisable to use different resolution datasets
824 such as borehole data and outcrop analogues to calibrate seismic results.

825 Open small-scale fracture networks mostly control the permeability characteristics of a
826 rock, developing the main conduits of fluid flow (e.g. Bush, 2010; Questiaux et al., 2010).
827 Conversely, when closed or cemented, they can provide barriers or baffles to fluid flow and
828 contribute to reservoir compartmentalisation (Damsleth et al., 1998; Steen et al., 1998;
829 Laubach, 2003; Maerten et al., 2006; Strijker et al., 2012). As suggested by Sanderson and
830 Nixon (2018), topological values of C_B and B_{22C} are important to understand parameters such
831 as permeability in a reservoir as they are related to connectivity and percolation. The
832 permeability of a rock and resulting fluid flow are mainly dependent on the fracture network
833 with topological values above the percolation threshold, assuming that fractures are conductive
834 (Fig. 11f, l). In contrast, permeability is dependent on the matrix where connectivity is below
835 the percolation threshold and fracture conductivity is lower than the matrix (Fig. 11f, l).

836 The analysis provided in this study is not limited to fractured reservoirs with hydrocarbon
837 accumulations, as our results and methodology could also be applied to other geoscience
838 disciplines such as geothermal reservoirs, hydrogeology, or carbon storage projects.

839 **6 Conclusions**

840 Carbonate platforms present complex multi-scale structural and sedimentological
841 characteristics as observed in Cariatiz (Fig. 4). The integration of fieldwork data with outcrop
842 exposure mapping and airborne LiDAR studies from Cariatiz, Spain, and 3D seismic data from
843 Pernambuco, Brazil, allowed a better understanding of multi-scale fracture networks developed
844 on carbonate platforms. These analyses reveal the complexity of fracture networks at different
845 scales and are useful to predict sub-seismic fractures from seismic datasets that are widely used

846 in industry. Fractures at each scale of observation behave differently, having different
847 geometrical and topological characteristics.

848 a) This study presented an integrated geometrical (orientation and branch length) and
849 topological (node, branch counting and dimensionless parameters) analysis of fracture
850 networks using a methodology in which small-, intermediate- and large- scale datasets
851 are combined.

852 b) Multi-scale fracture networks in carbonate platforms are complex; different fracture
853 types are identified at each scale of observation. At small scale, cm-long joints and
854 veins are mostly recognised (Fig. 12a). Fracture swarms are the dominant type observed
855 from airborne LiDAR, whereas km-long faults prevail at seismic scale (Fig. 12a).

856 c) Transitional scale gaps of fracture branch lengths between three scales of observation
857 (outcrop - airborne LiDAR, airborne LiDAR – seismic) are recognised. Fracture branch
858 lengths with sizes falling in these “transitional” gaps cannot be resolved by the
859 resolution of the analysed datasets. However, fractures of these lengths do exist in
860 nature, although datasets such as drone imagery and higher resolution seismic are
861 needed to bridge the gaps and allow fractures of all sizes to be measured (Fig. 12). This
862 issue is related to censoring and truncation effects.

863 d) Fracture branch orientation at intermediate (airborne LiDAR) and large (seismic) scales
864 appear to be controlled by the dominant orientation of the platform margin. Dominant
865 fracture sets observed in Cariatiz and Pernambuco strike parallel to the edge of the
866 platform margin. Fracture branches at outcrop scale (< 1 m) strike in almost all
867 directions, suggesting that different processes control the development of small
868 fractures (Fig. 10).

869 e) Fracture branch length distributions from Cariatiz and Pernambuco fit a negative
870 exponential or log-normal distribution in a massive, non-stratabound unit (Fig. 12).

871 This trend may be useful to predict sub-seismic branch lengths when working with
872 seismic datasets.

873 f) Fracture connectivity changes as a function of scale as it appears to decrease as fracture
874 length is increased (Fig. 11). This work complements the conclusions proposed by
875 Nixon et al (2012) in which they studied changes in connectivity at different
876 resolutions. Small-scale fracture branches measured at outcrop present higher
877 connectivity than larger fractures observed in LiDAR data. Fracture networks measured
878 from seismic data may show lower connectivity values compared to smaller fractures
879 expected at reservoir scale. This suggests that sub-seismic fracture networks mainly
880 control the permeability and fluid flow in reservoirs that are dominated by open
881 fractures or, instead, may develop barriers to fluid flow and contribute to reservoir
882 compartmentalisation when fractures are closed or cemented.

883 g) Outcrop data are useful to investigate the complexity of fracture networks and fracture
884 types that occur at sub-seismic scale. Understanding these sub-seismic parameters
885 allow us to better characterise fractured reservoirs.

886 **7 Acknowledgements**

887 The work contained in this paper is part of a PhD research supported by the Mexican
888 National Council of Science and Technology (CONACYT) and the hydrocarbon Secretariat of
889 Energy (SENER). We are thankful to the AAPG Grants-in-Aid General Fund Award 2018 to
890 cover fieldwork expenses. We would like to thank David Sanderson, an anonymous reviewer
891 and editor Cees Passchier for their thoughtful and useful comments and criticisms that helped
892 improve the manuscript. CGG is acknowledged for the provision of the Pernambuco 3D
893 seismic volume. The seismic data images are proprietary to and provided courtesy of CGG.
894 Schlumberger Petrel®, ESRI ArcGIS® and CorelDRAW® are also acknowledged for granting
895 academic licenses to Cardiff's 3D Seismic Lab.

896 **8 References**

- 897 Abotalib, A.Z., Heggy, E., Scabbia, G., Mazzoni, A., 2019. Groundwater dynamics in fossil
898 fractured carbonate aquifers in Eastern Arabian Peninsula: A preliminary investigation.
899 *Journal of Hydrology* 571, 460–470.
- 900 Adler, P.M., Thovert, J.-F., 1999. Fractures and fracture networks. Springer Science & Business
901 Media.
- 902 Alavian, S.A., Whitson, C.H., 2005. CO2 IOR Potential in Naturally Fractured Haft Kel Field, Iran.
903 International Petroleum Technology Conference. International Petroleum Technology
904 Conference.
- 905 Berkowitz, B., 2002. Characterizing flow and transport in fractured geological media: A review.
906 *Advances in Water Resources* 25, 861–884.
- 907 Bertotti, G., Hardebol, N., Taal-van Koppen, J.K., Luthi, S.M., 2007. Toward a quantitative
908 definition of mechanical units: New techniques and results from an outcropping deep-
909 water turbidite succession (Tanqua-Karoo Basin, South Africa). *AAPG Bulletin* 91, 1085–
910 1098.
- 911 Bonnet, E., Bour, B.O., Odling, N.E., Davy, P., Bour, O., Odling, N.E., Davy, P., Main, I., Cowie,
912 P., Berkowitz, B., 2001. Scaling of fracture systems in geological media. *Reviews of*
913 *Geophysics* 39, 347–383.
- 914 Bourbiaux, B., 2010. Fractured Reservoir Simulation: a Challenging and Rewarding Issue. *Oil*
915 *& Gas Science and Technology-Rev. IFP* 65, 227–238.
- 916 Braga, J.C., Martín, J.M., 1996. Geometries of reef advance in response to relative sea-level
917 changes in a Messinian (uppermost Miocene) fringing reef (Cariatiz reef, Sorbas Basin,

918 SE Spain). *Sedimentary Geology* 107, 61–81.

919 Brown, A.R., 2011. AAPG Memoir 42. Interpretation of three-dimensional seismic data,
920 Seventh. ed. Society of Exploration Geophysicists and American Association of
921 Petroleum Geologists, Tulsa, Oklahoma, U.S.A.

922 Buarque, B. V., Barbosa, J.A., Magalhães, J.R.G., Cruz Oliveira, J.T., Filho, O.J.C., 2016. Post-rift
923 volcanic structures of the Pernambuco Plateau, northeastern Brazil. *Journal of South
924 American Earth Sciences* 70, 251–267.

925 Buarque, B. V, Barbosa, J.A., Oliveira, J.T.C., Magalhães, J.R.G., Correia, O.J., Varella Buarque,
926 B., 2017. Carbonate Buildups in the Pernambuco Basin, NE Brazil. *An Acad Bras Cienc* 89,
927 841–857.

928 Burgess, P.M., Winefield, P., Minzoni, M., Elders, C., 2013. Methods for identification of
929 isolated carbonate buildups from seismic reflection data. *AAPG Bulletin* 97, 1071–1098.

930 Bush, I., 2010. An integrated approach to fracture characterisation., *Oil Review Middle East*
931 Issue Two 88–91.

932 Cacas, M.C., Daniel, J.M., Letouzey, J., 2001. Nested geological modelling of naturally
933 fractured reservoirs. *Petroleum Geoscience* 7, S43–S52.

934 Chen, Y., Ma, G., Wang, H., 2018. Heat extraction mechanism in a geothermal reservoir with
935 rough-walled fracture networks. *International Journal of Heat and Mass Transfer* 126,
936 1083–1093.

937 Chilès, J.-P., 2005. Stochastic modeling of natural fractured media: a review. *Geostatistics
938 Banff 2004*. Springer, 285–294.

- 939 Chopra, S., Marfurt, K.J., 2007. Seismic attributes for prospect identification and reservoir
940 characterization. Society of Exploration Geophysicists and European Association of
941 Geoscientists and Engineers.
- 942 Cowie, P.A., Knipe, R.J., Main, I.G., 1996. Introduction to the special issue. *Journal of Structural*
943 *Geology* 18, v–xi.
- 944 Cuevas Castell, J.M., Betzler, C., Rössler, J., Hüssner, H., Peinl, M., 2007. Integrating outcrop
945 data and forward computer modelling to unravel the development of a Messinian
946 carbonate platform in SE Spain (Sorbas Basin). *Sedimentology* 54, 423–441.
- 947 Damsleth, E., Sangolt, V., Aamodt, G., 1998. Sub-seismic Faults Can Seriously Affect Fluid Flow
948 in the Njord Field off Western Norway - A Stochastic Fault Modeling Case Study. SPE
949 Annual Technical Conference and Exhibition. Society of Petroleum Engineers.
- 950 Darros de Matos, R.M., 1999. History of the northeast Brazilian rift system: kinematic
951 implications for the break-up between Brazil and West Africa. Geological Society,
952 London, Special Publications 153, 55–73.
- 953 Dominguez, G.C., Fernando, S. V., Chilingarian, G. V., 1992. Chapter 12 Simulation of
954 Carbonate Reservoirs. *Developments in Petroleum Science* 30, 543–588.
- 955 Doornenbal, J.C., Kombrink, H., Bouroullec, R., Dalman, R.A.F., De Bruin, G., Geel, C.R.,
956 Houben, A.J.P., Jaarsma, B., Juez-Larré, J., Kortekaas, M., Mijnlief, H.F., Nelskamp, S.,
957 Pharaoh, T.C., Ten Veen, J.H., Ter Borgh, M., Van Ojik, K., Verreussel, R.M.C.H., Verweij,
958 J.M., Vis, G.-J., 2019. New insights on subsurface energy resources in the Southern North
959 Sea Basin area. Geological Society, London, Special Publications 494, SP494-2018–178.
- 960 dos Santos, E.J., Schmus, W.R. Van, Kozuch, M., Neves, B.B. de B., 2010. The Cariris Velhos

961 tectonic event in Northeast Brazil. *Journal of South American Earth Sciences* 29, 61–76.

962 Eberli, G.P., Anselmetti, F.S., Betzler, C., Van Konijnenburg, J.H., Bernoulli, D., 2005. Carbonate
963 platform to basin transitions on seismic data and in outcrops: Great Bahama Bank and
964 the Maiella Platform margin, Italy. *AAPG Memoir* 207–250.

965 Friedman, M., 1975. Fracture in rock. *Reviews of Geophysics* 13, 352.

966 Galvis, N.E.B., 2018. *Geomechanics, Fluid Dynamics and Well Testing, Applied to Naturally
967 Fractured Carbonate Reservoirs: Extreme Naturally Fractured Reservoirs*. Springer.

968 Gillespie, P.A., Walsh, J.J., Watterson, J., Bonson, C.G., Manzocchi, T., 2001. Scaling
969 relationships of joint and vein arrays from The Burren, Co. Clare, Ireland. *Journal of
970 Structural Geology* 23, 183–201.

971 Guerriero, V., Iannace, A., Mazzoli, S., Parente, M., Vitale, S., Giorgioni, M., 2010. Quantifying
972 uncertainties in multi-scale studies of fractured reservoir analogues: Implemented
973 statistical analysis of scan line data from carbonate rocks. *Journal of Structural Geology*
974 32, 1271–1278.

975 Gutmanis, J., Ardèvol i Oró, L., Díez-Canseco, D., Chebbihi, L., Awdal, A., Cook, A., 2018.
976 Fracture analysis of outcrop analogues to support modelling of the subseismic domain
977 in carbonate reservoirs, south-central Pyrenees. *Geological Society, London, Special
978 Publications* 459, 139–156.

979 Gutmanis, J.C., Ardèvol i Oró, L., 2015. Application of Pyrenean Fractured Carbonate Outcrops
980 for Subsurface Reservoir Characterisation. 77th EAGE Conference and Exhibition 2015.

981 Hermansen, H., Landa, G., Sylte, J., Thomas, L., 2000. Experiences after 10 years of
982 waterflooding the Ekofisk Field, Norway. *Journal of Petroleum Science and Engineering*

- 983 26, 11–18.
- 984 Jonk, R., Biermann, C., 2002. Deformation in Neogene sediments of the Sorbas and Vera
985 Basins (SE Spain): constraints on simple-shear deformation and rigid body rotation along
986 major strike-slip faults. *Journal of Structural Geology* 24, 963–977.
- 987 Kendall, C.G.S.C., Schlager, W., 1981. Carbonates and relative changes in sea level. *Marine*
988 *Geology* 44, 181–212.
- 989 Key, S.C., Agarwal, B., Sjøiland, G. V., Nielsen, H.H., 1999. Ekofisk Field redevelopment:
990 improved reservoir management through cross-discipline technology and integration of
991 three dimensional models. Geological Society, London, Petroleum Geology Conference
992 Series 5, 1147–1155.
- 993 Kim, Y.-S., Sanderson, D.J., 2005. The relationship between displacement and length of faults:
994 a review. *Earth-Science Reviews* 68, 317–334.
- 995 Kleipool, L.M., de Jong, K., de Vaal, E.L., Reijmer, J.J.G., 2017. Seismic characterization of
996 switching platform geometries and dominant carbonate producers (Miocene, Las
997 Negras, Spain). In: Della Porta, G. (Ed.), *Sedimentology* 64, 1676–1707.
- 998 Laubach, S.E., 2003. Practical approaches to identifying sealed and open fractures. *AAPG*
999 *Bulletin* 87, 561–579.
- 1000 Laubach, S.E., Olson, J.E., Gross, M.R., 2009. Mechanical and fracture stratigraphy. *AAPG*
1001 *Bulletin* 93, 1413–1426.
- 1002 Liu, R., Li, B., Jiang, Y., 2016. A fractal model based on a new governing equation of fluid flow
1003 in fractures for characterizing hydraulic properties of rock fracture networks. *Computers*
1004 *and Geotechnics* 75, 57–68.

- 1005 Lohr, T., 2004. Prediction of sub-seismic faults and fractures - integration of 3D seismic data,
1006 3D retro- deformation, and well data on an example of deformation around an inverted
1007 fault. *Seismic and Sub-Seismic Deformation on Different Scales in the NW German Basin*
1008 35–48.
- 1009 Loza Espejel, R., Alves, T.M.T.M., Blenkinsop, T.G.T.G., 2019. Distribution and growth styles of
1010 isolated carbonate platforms as a function of fault propagation. *Marine and Petroleum*
1011 *Geology In Press*, 484–507.
- 1012 Maerten, L., Gillespie, P., Daniel, J.-M., 2006. Three-dimensional geomechanical modeling for
1013 constraint of subseismic fault simulation. *AAPG Bulletin* 90, 1337–1358.
- 1014 Magalhães, J.R., Barbosa, J.A., Oliveira, J.T.C., Lima Filho, M.F., 2014. Characterization of the
1015 ocean-continent transition in the Paraíba basin and Natal platform region, NE Brazil.
1016 *Revista Brasileira de Geofísica* 32 (3), 481–496.
- 1017 Mandujano, J.J., Khachaturov, R.V., Tolson, G., Duncan Keppie, J., 2005. Curvature analysis
1018 applied to the Cantarell structure, southern Gulf of Mexico: implications for hydrocarbon
1019 exploration. *Computers & Geosciences* 31, 641–647.
- 1020 Manzocchi, T., 2002. The connectivity of two-dimensional networks of spatially correlated
1021 fractures. *Water Resources Research* 38, 1-1-1–20.
- 1022 Manzocchi, T., Walsh, J.J., Bailey, W.R., 2009. Population scaling biases in map samples of
1023 power-law fault systems. *Journal of Structural Geology* 31, 1612–1626.
- 1024 March, R., Doster, F., Geiger, S., 2018. Assessment of CO₂ Storage Potential in Naturally
1025 Fractured Reservoirs With Dual-Porosity Models. *Water Resources Research* 54, 1650–
1026 1668.

- 1027 Marfurt, K.J., Alves, T.M., 2015. Pitfalls and limitations in seismic attribute interpretation of
1028 tectonic features. *Interpretation* 3, SB5–SB15.
- 1029 Martín, J., Braga, J.C., 1994. Messinian events in the Sorbas Basin in southeastern Spain and
1030 their implications in the recent history of the Mediterranean. *Sedimentary Geology* 90,
1031 257–268.
- 1032 Mauldon, M., Dunne, W.M., Rohrbaugh, M.B., 2001. Circular scanlines and circular windows:
1033 new tools for characterizing the geometry of fracture traces. *Journal of Structural*
1034 *Geology* 23, 247–258.
- 1035 Medici, G., West, L.J., Banwart, S.A., 2019. Groundwater flow velocities in a fractured
1036 carbonate aquifer-type: Implications for contaminant transport. *Journal of Contaminant*
1037 *Hydrology* 222, 1–16.
- 1038 Meijninger, B.M.L., Vissers, R.L.M., 2006. Miocene extensional basin development in the Betic
1039 Cordillera, SE Spain revealed through analysis of the Alhama de Murcia and Crevillente
1040 Faults. *Basin Research* 18, 547–571.
- 1041 Morley, C.K., Nixon, C.W., 2016. Topological characteristics of simple and complex normal
1042 fault networks. *Journal of Structural Geology* 84, 68–84.
- 1043 Munro, M.A., Blenkinsop, T.G., 2012. MARD-A moving average rose diagram application for
1044 the geosciences. *Computers and Geosciences* 49, 112–120.
- 1045 Needham, T., Yielding, G., Fox, R., 1996. Fault population description and prediction using
1046 examples from the offshore U.K. *Journal of Structural Geology* 18, 155–167.
- 1047 Nelson, R.A., 2001. *Geologic analysis of naturally fractured reservoirs*, 2nd Edition. Gulf
1048 Professional Pub.

- 1049 Nicol, A., Walsh, J.J.J., Watterson, J., Gillespie, P.A.A., 1996. Fault size distributions - Are they
1050 really power-law? *Journal of Structural Geology* 18, 191–197.
- 1051 Nixon, C.W., Sanderson, D.J., Bull, J.M., 2012. Analysis of a strike-slip fault network using high
1052 resolution multibeam bathymetry, offshore NW Devon U.K. *Tectonophysics* 541–543,
1053 69–80.
- 1054 Nooitgedacht, C.W., Kleipool, L.M., Andeweg, B., Reolid, J., Betzler, C., Lindhorst, S., Reijmer,
1055 J.J.G., 2018. New insights in the development of syn-depositional fractures in rimmed
1056 flat-topped carbonate platforms, Neogene carbonate complexes, Sorbas Basin, SE Spain.
1057 *Basin Research* 30, 596–612.
- 1058 Nyberg, B., Nixon, C.W., Sanderson, D.J., 2018. NetworkGT: A GIS tool for geometric and
1059 topological analysis of two-dimensional fracture networks. *Geosphere* 14, 1618–1634.
- 1060 Odling, N.E., 1997. Scaling and connectivity of joint systems in sandstones from western
1061 Norway. *Journal of Structural Geology* 19, 1257–1271.
- 1062 Odling, N.E., Gillespie, P., Bourguine, B., Castaing, C., Chiles, J.P., Christensen, N.P., Fillion, E.,
1063 Genter, A., Olsen, C., Thrane, L., Trice, R., Aarseth, E., Walsh, J.J., Watterson, J., 1999.
1064 Variations in fracture system geometry and their implications for fluid flow in fractures
1065 hydrocarbon reservoirs. *Petroleum Geoscience* 5, 373–384.
- 1066 Peacock, D.C.P., Knipe, R.J., Sanderson, D.J., 2000. Glossary of normal faults. *Journal of*
1067 *Structural Geology* 22, 291–305.
- 1068 Peacock, D.C.P., Nixon, C.W., Rotevatn, A., Sanderson, D.J., Zuluaga, L.F., 2016. Glossary of
1069 fault and other fracture networks. *Journal of Structural Geology* 92, 12–29.
- 1070 Pickering, G., Peacock, D.C.P., Sanderson, D.J., Bull, J.M., 1997. Modeling tip zones to predict

- 1071 the throw and length characteristics of faults. AAPG Bulletin 81, 82–99.
- 1072 Procter, A., Sanderson, D.J., 2018. Spatial and layer-controlled variability in fracture networks.
1073 Journal of Structural Geology 108, 52–65.
- 1074 Questiaux, J.-M., Couples, G.D., Ruby, N., 2010. Fractured reservoirs with fracture corridors.
1075 Geophysical Prospecting 58, 279–295.
- 1076 Reolid, J., Betzler, C., Braga, J.C., Martín, J.M., Lindhorst, S., Reijmer, J.J.G., 2014. Reef slope
1077 geometries and facies distribution: controlling factors (Messinian, SE Spain). Facies 60,
1078 737–753.
- 1079 Riding, R., Martin, J.M., Braga, J.C., 1991. Coral-stromatolite reef framework, Upper Miocene,
1080 Almeria, Spain. Sedimentology 38, 799–818.
- 1081 Rohrbaugh, M.B., Dunne, W.M., Mauldon, M., 2002. Estimating fracture trace intensity,
1082 density, and mean length using circular scan lines and windows. AAPG Bulletin 86, 2089–
1083 2104.
- 1084 Sánchez-Almazo, I.M., Braga, J.C., Dinarès-Turell, J., Martín, J.M., Spiro, B., 2007.
1085 Palaeoceanographic controls on reef deposition: the Messinian Cariatiz reef (Sorbas
1086 Basin, Almería, SE Spain). Sedimentology 54, 637–660.
- 1087 Sanderson, D.J., 2016. Field-based structural studies as analogues to sub-surface reservoirs.
1088 Geological Society, London, Special Publications 436, 207–217.
- 1089 Sanderson, D.J., Nixon, C.W., 2018. Topology, connectivity and percolation in fracture
1090 networks. Journal of Structural Geology 115, 167–177.
- 1091 Sanderson, D.J., Nixon, C.W., 2015. The use of topology in fracture network characterization.

- 1092 Journal of Structural Geology 72, 55–66.
- 1093 Sanderson, D.J., Peacock, D.C.P., Nixon, C.W., Rotevatn, A., 2019. Graph theory and the
1094 analysis of fracture networks. Journal of Structural Geology 125, 155–165.
- 1095 Santiago, E., Velasco-Hernández, J.X., Romero-Salcedo, M., 2014. A methodology for the
1096 characterization of flow conductivity through the identification of communities in
1097 samples of fractured rocks. Expert Systems with Applications 41, 811–820.
- 1098 Sarkheil, H., Hassani, H., Alinia, F., 2013. Fractures distribution modeling using fractal and
1099 multi-fractal–neural network analysis in Tabnak hydrocarbon field, Fars, Iran. Arabian
1100 Journal of Geosciences 6, 945–956.
- 1101 Steen, Ø., Sverdrup, E., Hanssen, T.H., 1998. Predicting the distribution of small faults in a
1102 hydrocarbon reservoir by combining outcrop, seismic and well data. Geological Society,
1103 London, Special Publications 147, 27–50.
- 1104 Strijker, G., Bertotti, G., Luthi, S.M., 2012. Multi-scale fracture network analysis from an
1105 outcrop analogue: A case study from the Cambro-Ordovician clastic succession in Petra,
1106 Jordan. Marine and Petroleum Geology 38, 104–116.
- 1107 Tao, Z., Alves, T.M., 2019. Impacts of data sampling on the interpretation of normal fault
1108 propagation and segment linkage. Tectonophysics 762, 79–96.
- 1109 TerHeege, J.H., Osinga, S., Carpentier, S., 2018. The Geomechanical Response of Naturally
1110 Fractured Carbonate Reservoirs to Operation of a Geothermal Doublet.
- 1111 Torabi, A., Berg, S.S., 2011. Scaling of fault attributes: A review, Marine and Petroleum
1112 Geology. Elsevier.

- 1113 Van As, A., Jeffrey, R.G., 2002. Hydraulic fracture growth in naturally fractured rock: mine
1114 through mapping and analysis.
- 1115 Vidal, J., Genter, A., 2018. Overview of naturally permeable fractured reservoirs in the central
1116 and southern Upper Rhine Graben: Insights from geothermal wells. *Geothermics* 74, 57–
1117 73.
- 1118 Vollmer, F.W., 2015. Orient 3: a new integrated software program for orientation data
1119 analysis, kinematic analysis, spherical projections, and Schmidt plots. *Geological Society*
1120 *of America Abstracts with Programs*. 49.
- 1121 Vollmer, F.W., 1995. C program for automatic contouring of spherical orientation data using
1122 a modified Kamb method. *Computers and Geosciences* 21, 31–49.
- 1123 Vollmer, F.W., 1990. An application of eigenvalue methods to structural domain analysis. *GSA*
1124 *Bulletin* 102, 786–791.
- 1125 Watkins, H., Bond, C.E., Healy, D., Butler, R.W.H., 2015. Appraisal of fracture sampling
1126 methods and a new workflow to characterise heterogeneous fracture networks at
1127 outcrop. *Journal of Structural Geology* 72, 67–82.
- 1128 Watterson, J., Walsh, J.J., Gillespie, P.A., Easton, S., 1996. Scaling systematics of fault sizes on
1129 a large-scale range fault map. *Journal of Structural Geology* 18, 199–214.
- 1130 Zampetti, V., Schlager, W., van Konijnenburg, J.-H., Everts, A.-J., 2004. Architecture and
1131 growth history of a Miocene carbonate platform from 3D seismic reflection data; Luconia
1132 province, offshore Sarawak, Malaysia. *Marine and Petroleum Geology* 21, 517–534.
- 1133 Zarei, H.R., Uromeihy, A., Sharifzadeh, M., 2012. Identifying geological hazards related to
1134 tunneling in carbonate karstic rocks - Zagros, Iran. *Arabian Journal of Geosciences* 5,

1135 457–464.

1136 Zeeb, C., Gomez-Rivas, E., Bons, P.D., Blum, P., 2013. Evaluation of Sampling methods for
1137 fracture network characterization using Outcrops. AAPG Bulletin 97, 1545–1566.

1138

POSTPRINT

1139 **9 Figure captions**

1140 Figure 1. a) Location of the study area in SE Spain. b) Regional map of the Sorbas Basin
1141 showing the Messinian Reef Unit, and the area of interest at Cariatiz. Modified after Reolid et
1142 al. (2014). c) Topographic map showing the field sites where fracture network mapping was
1143 performed using the augmented circular scanline method of Watkins et al. (2015). Rose
1144 diagrams show the main fracture orientation at each site.

1145 Figure 2. a) Location map of the study area in the Pernambuco Basin. b) Variance depth
1146 slice (-1720 m) showing the area (yellow line) where fracture characterisation was performed.
1147 c) Seismic section across the Pernambuco Platform showing its internal geometry and seismic
1148 facies, as well as the presence of normal faults. *Sequence numbers after Buarque et al (2017).
1149 Scale and exact location cannot be given due to data privacy.

1150 Figure 3. Flowchart summarising the methodology used in this work to obtain fracture
1151 data from different datasets. Three different input datasets with distinct scale-resolution were
1152 utilised (outcrop: small scale, LiDAR: intermediate scale, seismic: large scale). *Consider
1153 suggestions by Rohrbaugh et al. (2002) and Watkins et al. (2015) to determine the radius (r).
1154 See more details in the text.

1155 Figure 4. Outcrop images and facies model showing the complexity of structural and
1156 depositional attributes in the Cariatiz fringing reef unit. a) Outcrop image showing large
1157 fractures across the platform edge. b) Enlarged photo showing circular shapes of *Porites* on a
1158 horizontal section. c) Fracture swarms along the platform margin. See Fig. 6a for location. d)
1159 Facies model of Cariatiz, modified after Braga and Martín (1996) and Reolid et al. (Braga and
1160 Martín, 1996; Reolid et al., 2014). e) Outcrop photo showing vertical *Porites*. See Fig. 1c for
1161 location.

1162 Figure 5. Rectified photographs of circular scanlines showing the fracture networks
1163 collected at outcrop in Cariatiz. a-j) Digitised fracture networks showing the topological
1164 parameters. Circular scanline (red line), fracture intersections with the sampling circle (yellow
1165 circle), I nodes (green triangles), Y nodes (blue squares), X nodes (orange hexagons). k) Field
1166 photograph showing the grid used to rectify the perspective of the circle. l) Rectified photo
1167 where geometrical and topological analyses can be performed.

1168 Figure 6. LiDAR map of the study area in the Cariatiz carbonate platform with the slope
1169 attribute highlighting discontinuities. Fractures present high slope values. Site locations are
1170 shown with red circles. a) Uninterpreted 3D visualisation of the LiDAR map, useful to locate
1171 outcrop localities and perform fracture interpretation in the intermediate scale. b) Interpreted
1172 map showing fracture branches as black lines as well as fracture nodes. The map was divided
1173 into three zones to analyse fracture variability.

1174 Figure 7. Schematic diagrams showing the topological analysis and sampling effects of
1175 fracture networks. a) Fracture traces (A-B and C-D) and their node and branch association with
1176 intersecting fractures (dashed lines). I-nodes (green circles); Y-nodes (blue triangles); X-nodes
1177 (orange diamonds); I-I or isolated branch (I-I nodes with no fracture intersection); I-C or partly
1178 connected branch (I-Y or I-X node intersection); and C-C or doubly connected branch (Y-Y,
1179 Y-X, or X-X node intersection). Modified from Sanderson and Nixon (2015). b) Erroneous
1180 recognition of fracture traces occurs as they can be interpreted differently depending on the
1181 criteria used, leading to inconsistent trace lengths and orientations depending on the interpreter.
1182 c) By utilising fracture branches as a result of topological analyses, the fracture segments can
1183 be identified easier, resulting in reliable measurements of geometrical characteristics. d)
1184 Truncation effects occur due to limits in data resolution, and it is present regardless of the use
1185 of branches or traces. e) Censoring effects occur as the fractures extend the observable area. f)

1186 Censoring effects can be minimised by the use of fracture branches as they do not include the
1187 entire trace; rather only one segment of the trace.

1188 Figure 8. Seismic depth slices of the Pernambuco carbonate shelf on the variance attribute
1189 computed in this work. Fracture interpretation was performed within an area of interest every
1190 100 m in depth from Z=-1020 m to Z=-2020 m. Topological analyses were also carried out to
1191 better understand the fracture network. Fractures are represented with continuous pink lines. I
1192 nodes are represented by green triangles, Y nodes by blue squares, and X nodes by orange
1193 hexagons. Seismic images are rotated and therefore not in their original orientation due to data
1194 protection.

1195 Figure 9. Statistical plots showing fracture branch length distribution from three scale
1196 datasets. Outcrop data from the Cariatiz carbonate platform is plotted in yellow. LiDAR data
1197 from the Cariatiz carbonate platform is plotted in green. Seismic data from the Pernambuco
1198 carbonate platform is plotted in blue. a), f) and k) Histograms showing a positive skew
1199 distribution. b), g) and l) Box plots showing the concentration of branch lengths. Q1, Q2 and
1200 Q3 are the values for the lower quartile, median and upper quartile. Box represents the
1201 interquartile range, thick solid grey line represents the minimum and maximum values
1202 (whiskers), and dotted line shows the outliers of the data. c), h) and m) Cumulative percentage
1203 plotted against fracture branch length; note good fit to a straight line for small branch lengths.
1204 d), i) and n) Log (cumulative percentage) plotted against fracture branch length, with straight
1205 line indicating negative exponential distribution. e), j) and o) Log (cumulative percentage)
1206 plotted against log (fracture branch length), with straight line indicating power-law distribution.
1207 Straight red line indicates a good fit.

1208 Figure 10. Bi-directional moving average rose diagrams and numerical cluster analysis
1209 showing fracture orientation and fracture sets from (a and d) outcrop, (b and e) LiDAR, and (c

1210 and f) seismic data. Rose diagrams were generated as equal area with a weighting factor of 0.9
1211 and aperture of 9° . Equal area rose diagrams are used to visualise results from the cluster
1212 analyses.

1213 Figure 11. Triangular plots showing detailed topological analyses of nodes and branches
1214 and resulting parameters from different scales of observation. a) to f) Outcrop and LiDAR
1215 topological results from the Cariatiz Fringing Reef Unit. g) to l) Seismic topological results
1216 from the Pernambuco carbonate platform. Yellow area represents the variation in results from
1217 outcrop data. Green area represents the variation in results from LiDAR maps. Similarly, blue
1218 area represents the variation in results from seismic data. *Purple area is an interpretation of
1219 topological values expected with branch lengths observable at seismic scale in Cariatiz.
1220 **Orange area is an interpretation of expected values at sub-seismic scale in Pernambuco
1221 assuming that fracture connectivity increases at a smaller scale, similarly to the observed trend
1222 in Cariatiz. a, g) Fracture network node classification. Yellow circle: average value from
1223 outcrop data; green triangle: average value from LiDAR data; and blue square: average value
1224 from seismic data. b, h) N_B/N_L ratio shows values of 3 for outcrop data, 2 for LiDAR data, and
1225 2.5 for seismic data. c, i) Average number of connections per line (C_L) shows a value of 3.4 at
1226 outcrop level, a value of 2 from LiDAR data, and a value of 2.6 from seismic data. d, j) Average
1227 number of connections per branch (C_B) with a value of 1.82 at outcrop scale, 1.49 at LiDAR
1228 scale, and 1.66 at seismic scale. e, k) Branch classification with I-I isolated branches, I-C partly
1229 connected branches, and C-C doubly connected branches. f, l) Dimensionless intensity of
1230 branches at percolation (B_{22C}).

1231 Figure 12. Multi-scale statistics of fracture branch lengths and figures showing different
1232 fracture types with associated datasets depending on scale. a) Outcrop photos with associated
1233 datasets and box plots showing the distribution of fracture branch lengths between different
1234 datasets. It is observed from the box plots that there is no overlap between datasets (outcrop -

1235 airborne LiDAR and airborne LiDAR - seismic). Large fractures with a scale between outcrop
1236 and airborne LiDAR were recognised in the field and can be mapped with the use of ground
1237 LiDAR or drone imagery. Fractures observed at each scale are mainly of a different type. Veins
1238 and joints can be mapped at outcrop; fracture swarms can be mapped with airborne LiDAR
1239 maps; and large kilometre faults can be mapped by using seismic data. Fractures with a branch
1240 size in between the scale of the three studied datasets can be mapped with data of different
1241 resolution such as drone imagery and higher resolution seismic. b) Cumulative percentage
1242 plotted against fracture branch length; note good fit to a straight line for small branch lengths.
1243 c) Log (cumulative percentage) plotted against fracture branch length, with straight line
1244 indicating negative exponential distribution. d) Log (cumulative percentage) plotted against
1245 log (fracture branch length), with straight line indicating power-law distribution. Straight red
1246 line represents a good fit.

1247 **10 Appendices' captions**

1248 Figure A1. Fracture branch length histograms from the Cariatiz carbonate platform. a) to
1249 j) Histograms from outcrop localities. k) to m) Histograms from LiDAR zones.

1250 Figure A2. Fracture branch length histograms from seismic data (depth slices -1020 m to
1251 -2020 m) in the Pernambuco carbonate platform. Fracture branches at seismic scale are in the
1252 range of hundreds of metres.

1253 Figure B1. Bi-directional moving average rose diagrams showing fracture orientation
1254 from the Cariatiz carbonate platform. a) to j) Rose diagrams from outcrop localities. k) to m)
1255 Rose diagrams from LiDAR zones. Rose diagrams were generated as equal area with a
1256 weighting factor of 0.9 and aperture of 9°.

1257 Figure B2. Bi-directional moving average rose diagrams showing fracture orientation
1258 from our study area in the Pernambuco carbonate platform at different seismic slices from Z=

1259 -1020 m to -2020 m. Rose diagrams were generated as equal area with a weighting factor of
1260 0.9 and aperture of 9°.

1261 Figure C1. Triangular plots showing detailed topological analyses of nodes and branches
1262 from outcrop localities and LiDAR zones at the Cariatiz Fringing Reef (a to f), as well as
1263 seismic depth slices from the Pernambuco carbonate platform (g to l). Yellow, green and blue
1264 shapes represent the range of node and branch values at outcrop, LiDAR and seismic scale,
1265 respectively. a, g) Fracture network node classification. b, h) N_B/N_L ratio shows most of the
1266 points lying over N_B/N_L ratio value of 3 within the range of 2 and 4. c, i) Average number of
1267 connections per line (C_L) showing that in Cariatiz, at outcrop level, values range from 2 to 5.
1268 d, j) Average number of connections per branch (C_B). e, k) Branch classification with I-I
1269 isolated branches, I-C partly connected branches, and C-C doubly connected branches. f, l)
1270 Dimensionless intensity of branches (B_{22C}).

1271 Table D1. Summary of topological parameters, notation, and key equations. Modified
1272 from Sanderson and Nixon (2015, 2018).

1273 Table D2. Fracture topological results from field data (outcrop and LiDAR) and seismic
1274 data.

Figure 1

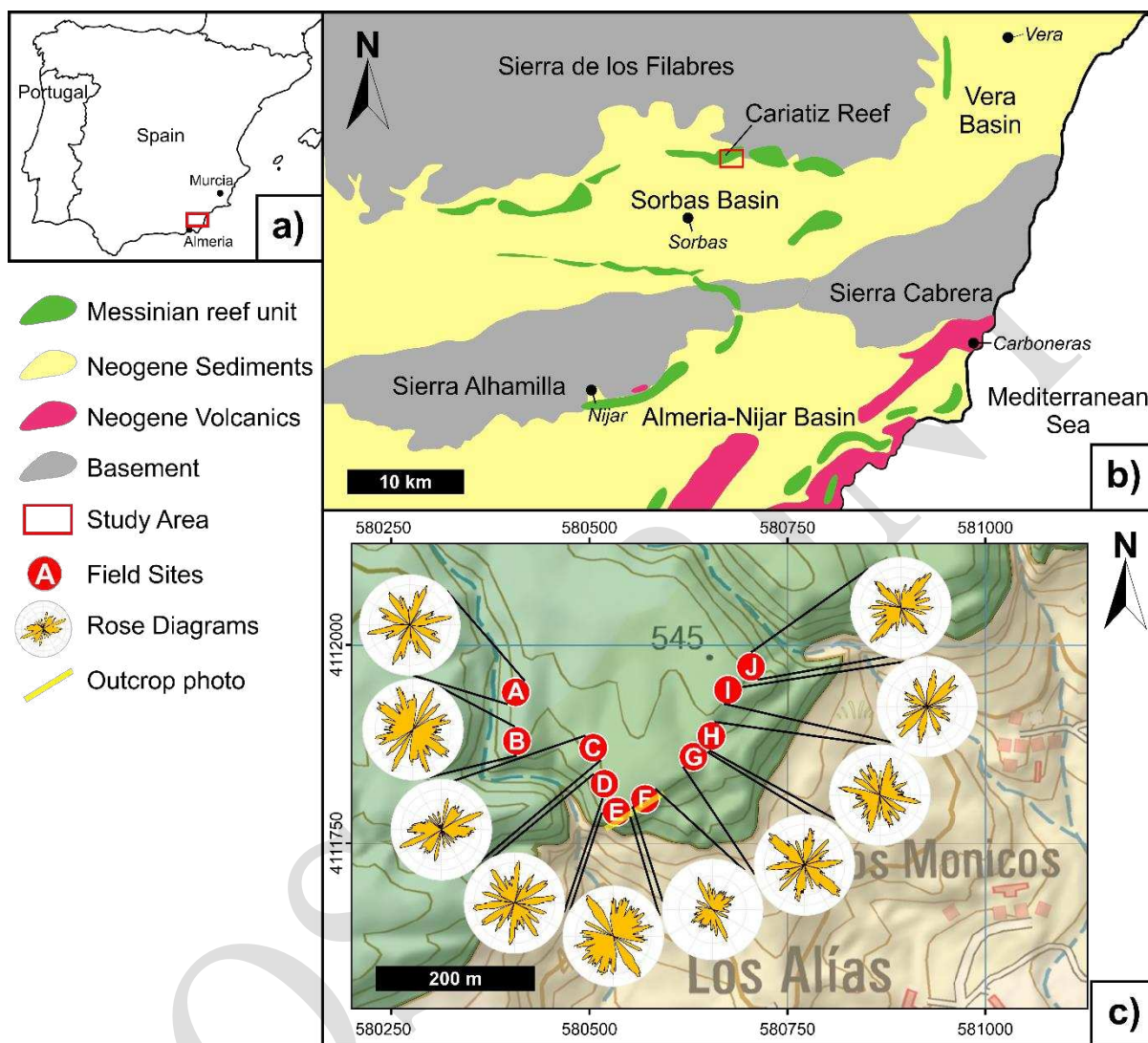
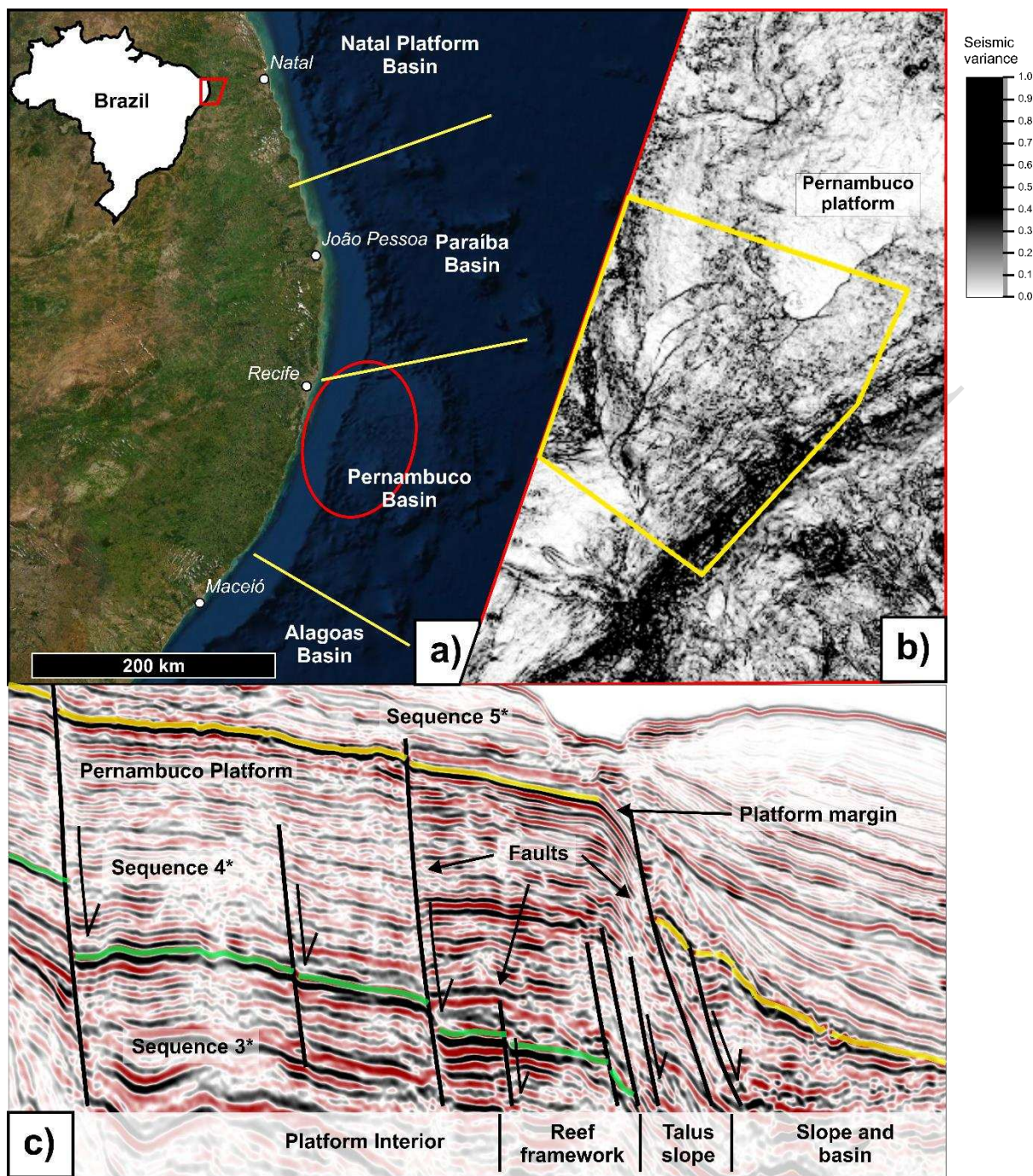


Figure 2



1285

1286

1287

1288

1289

Figure 3

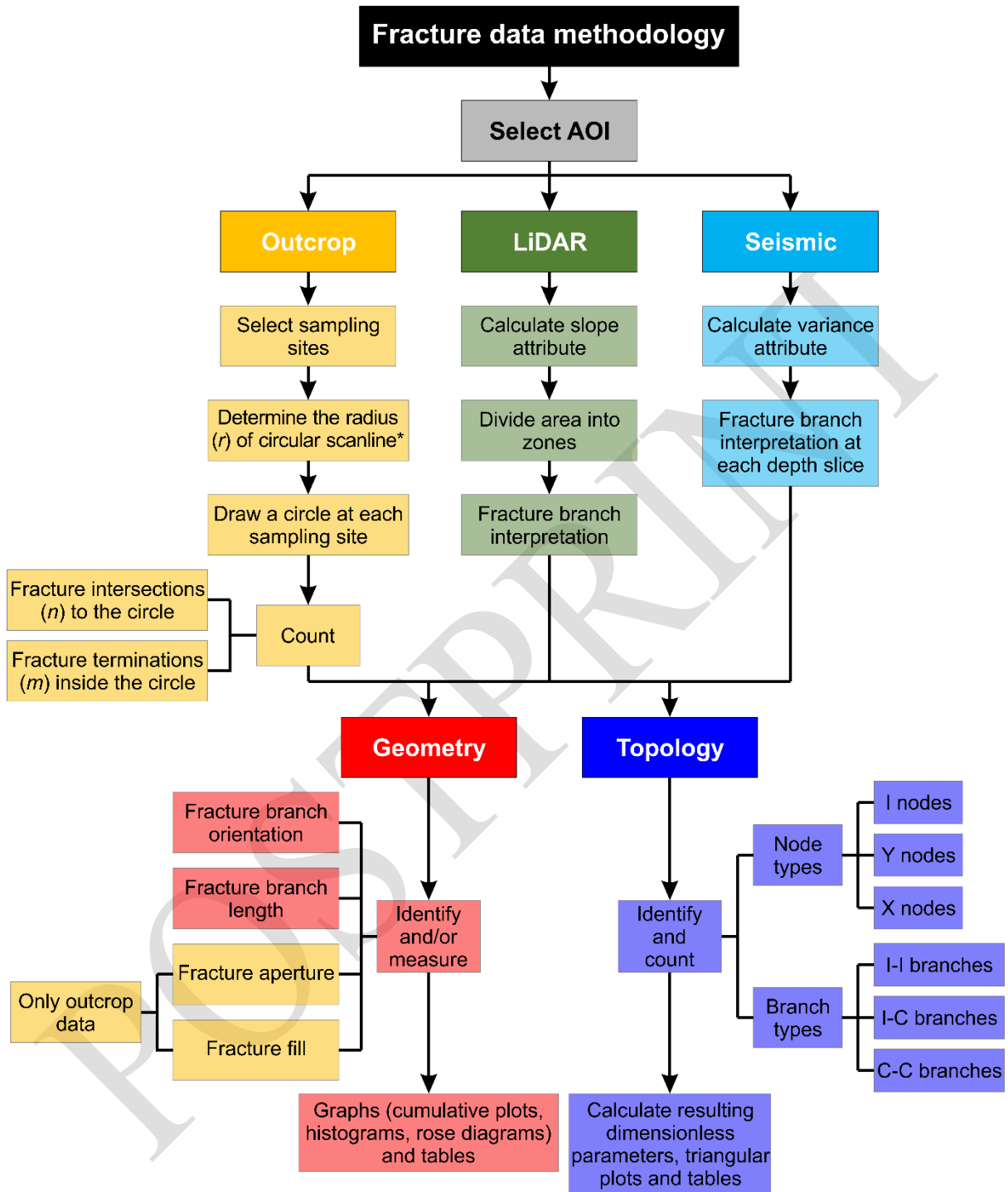
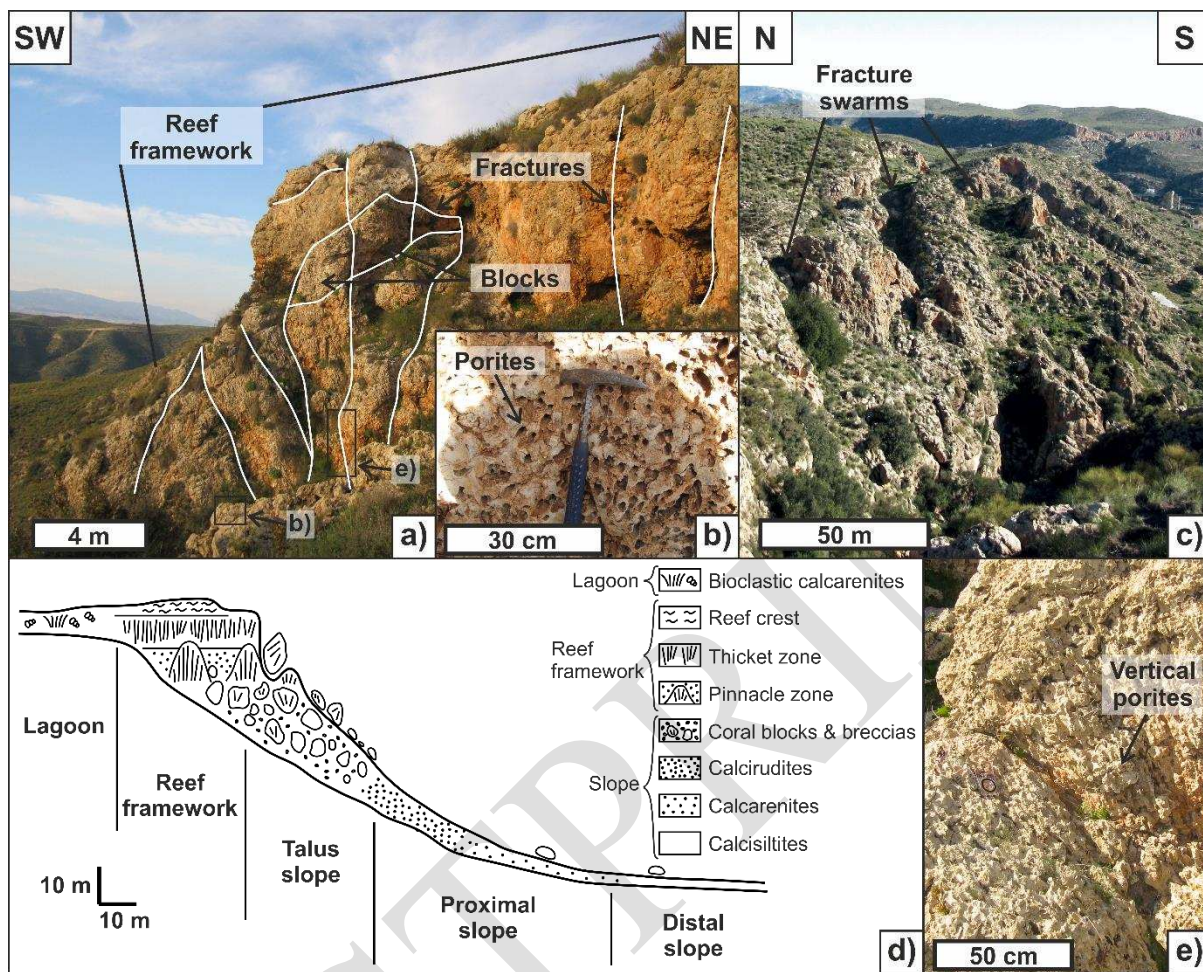


Figure 4



1296

1297

1298

1299

1300

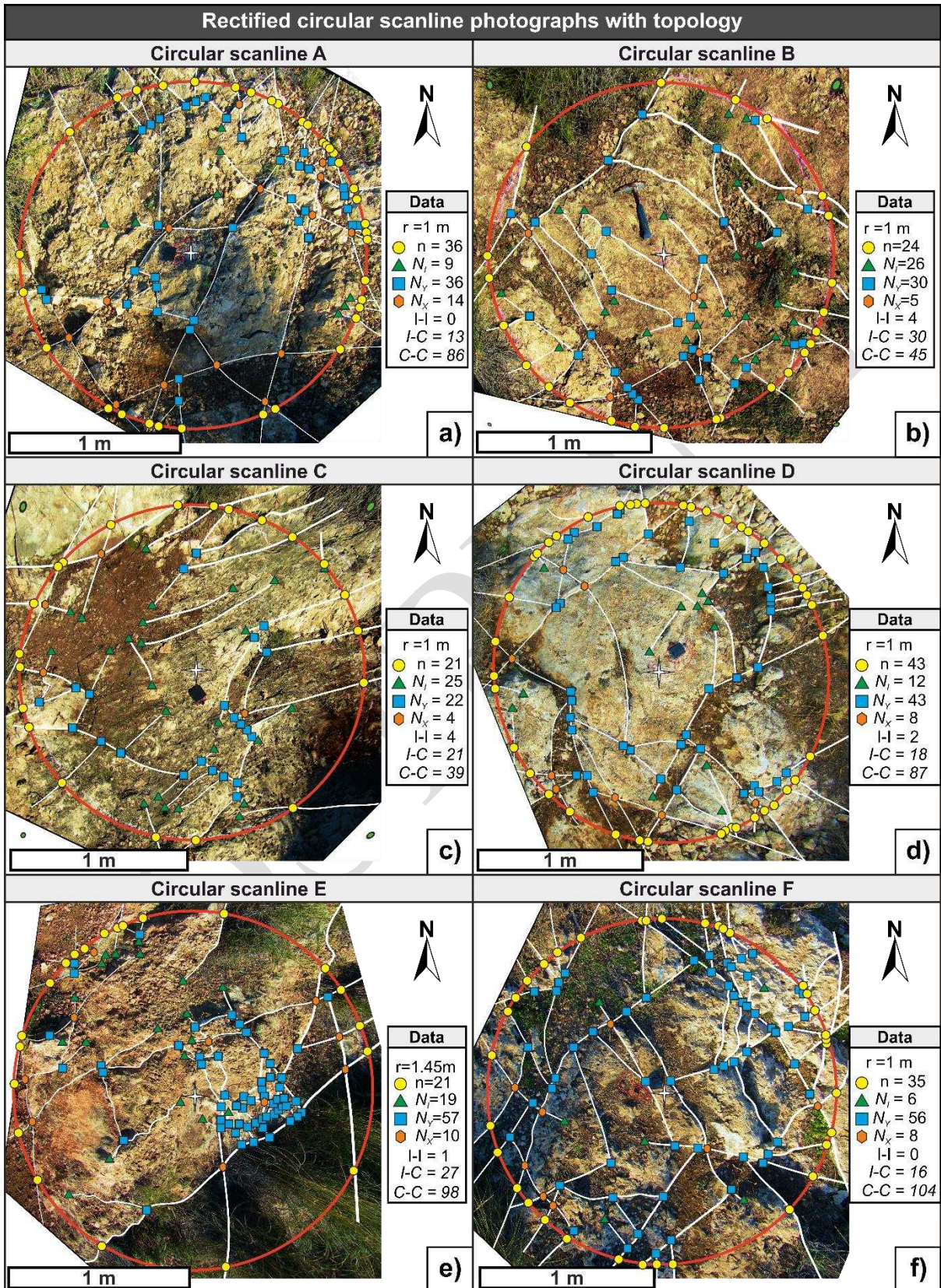
1301

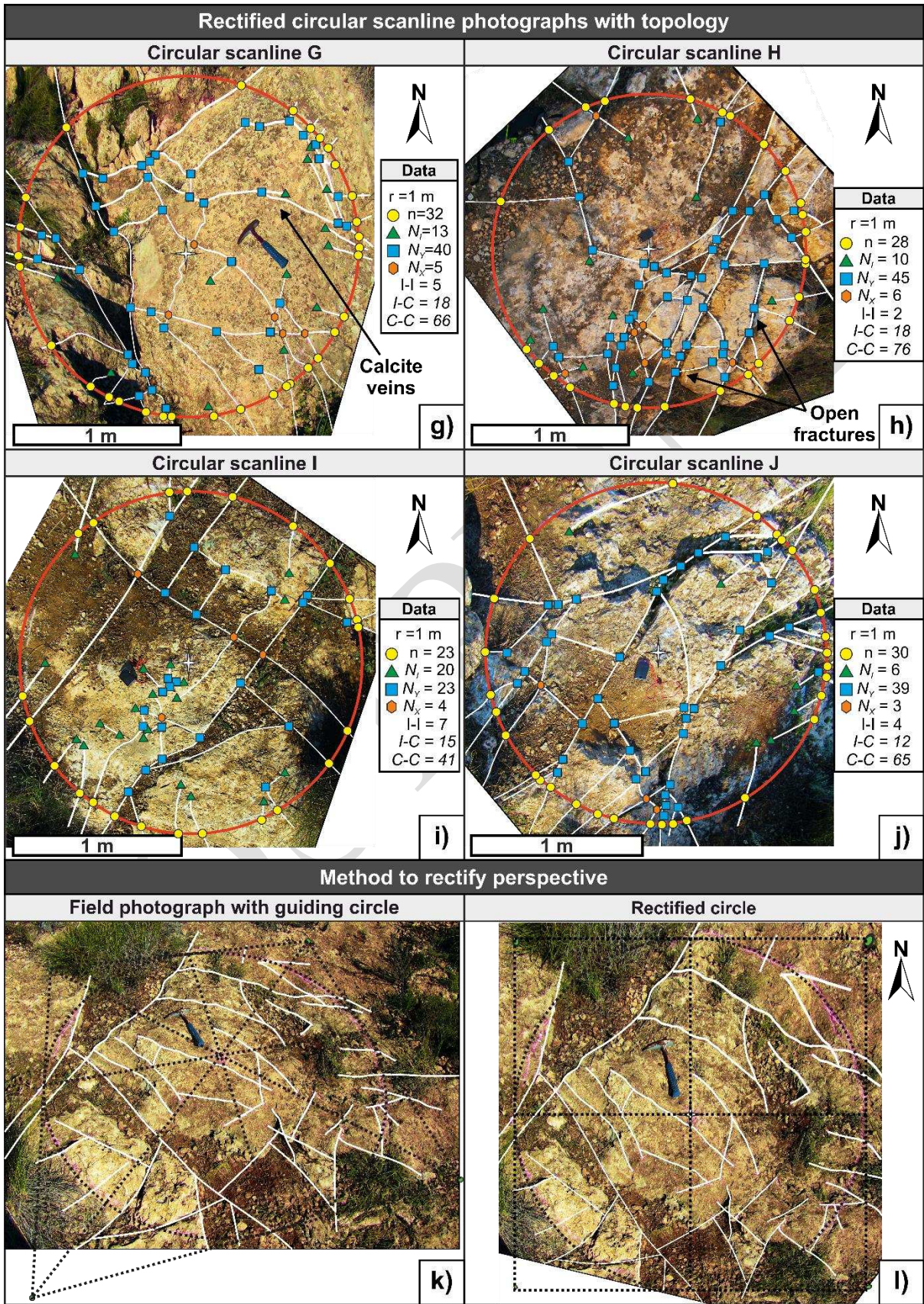
1302

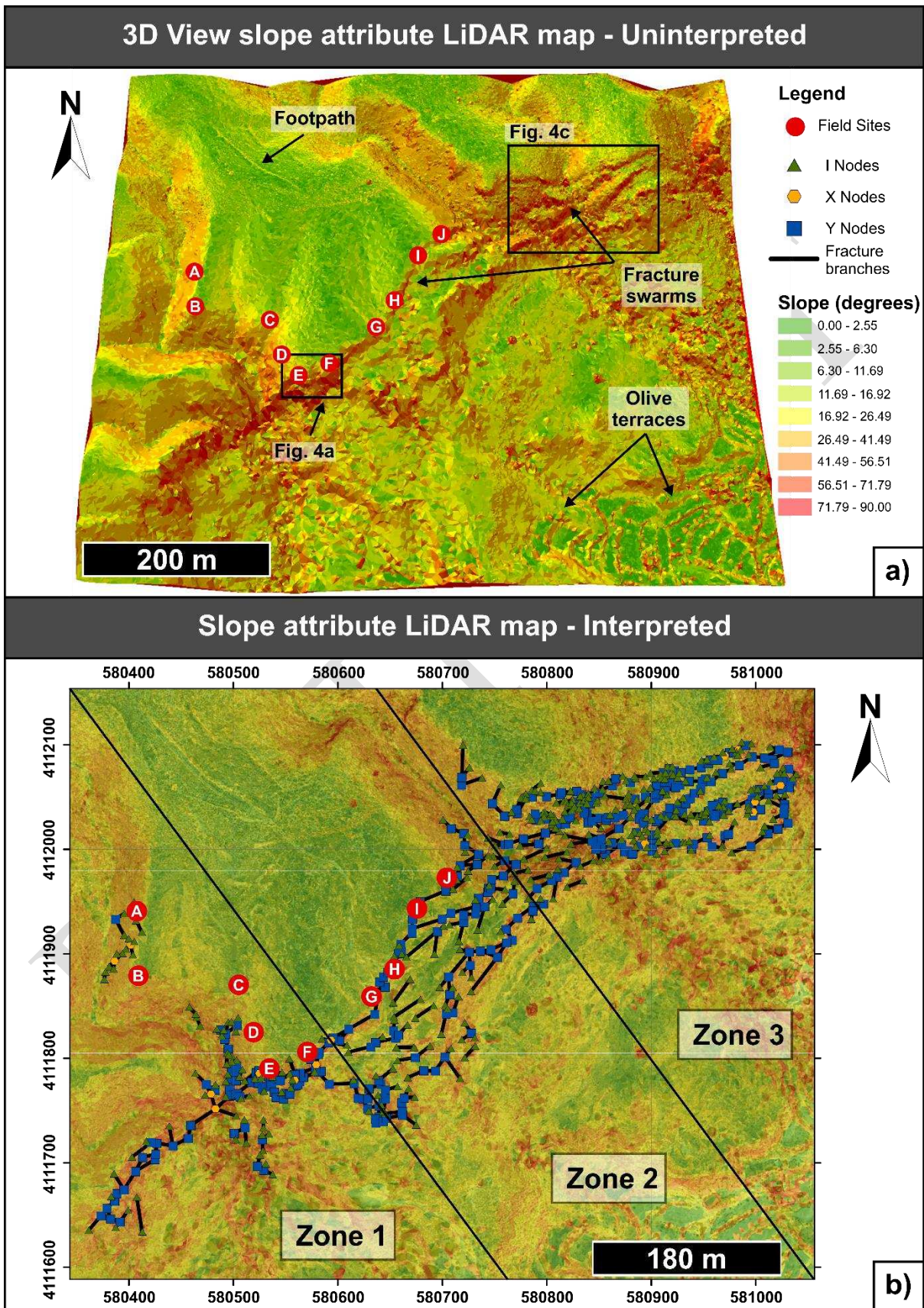
1303

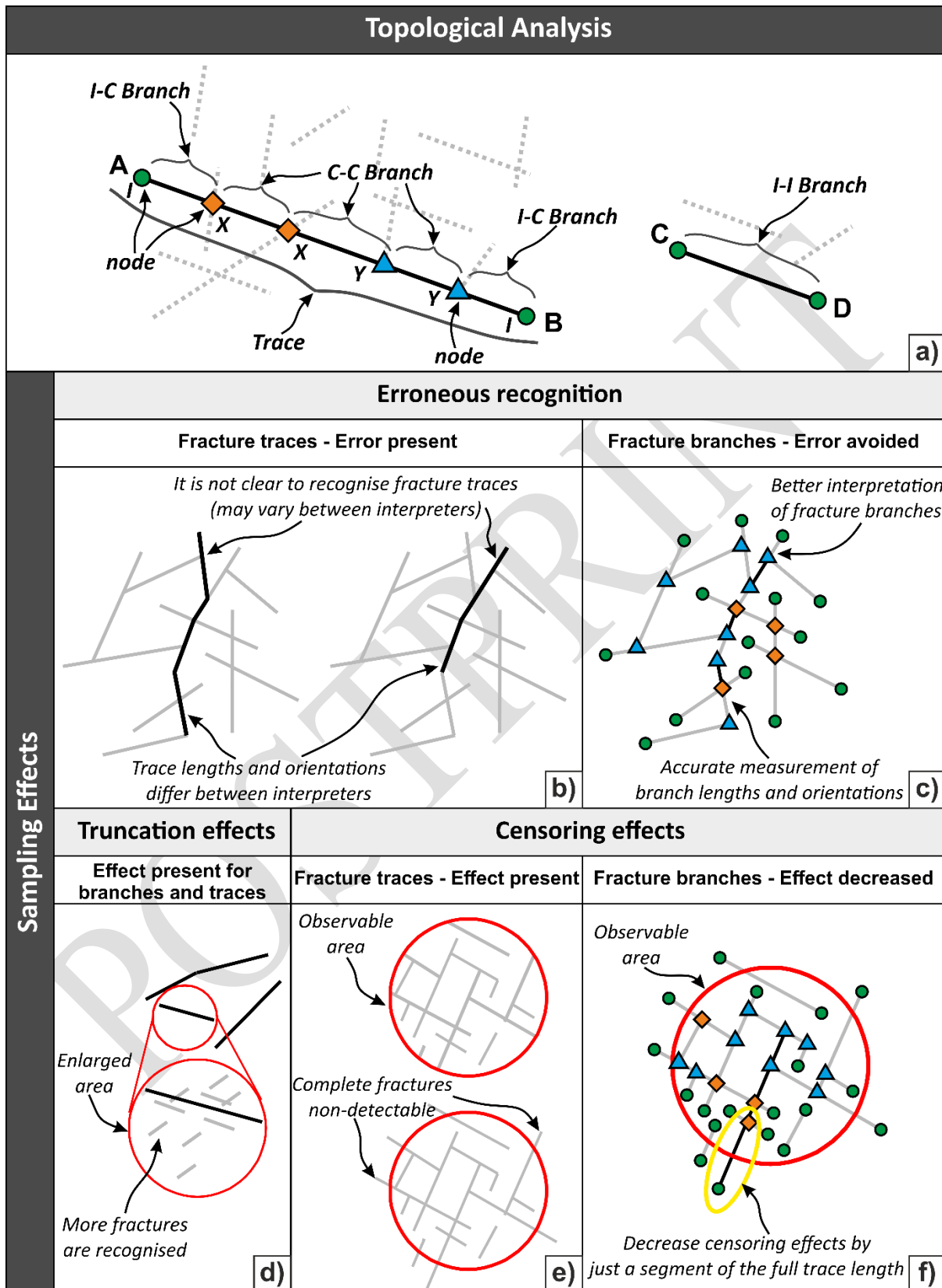
1304

Figure 5



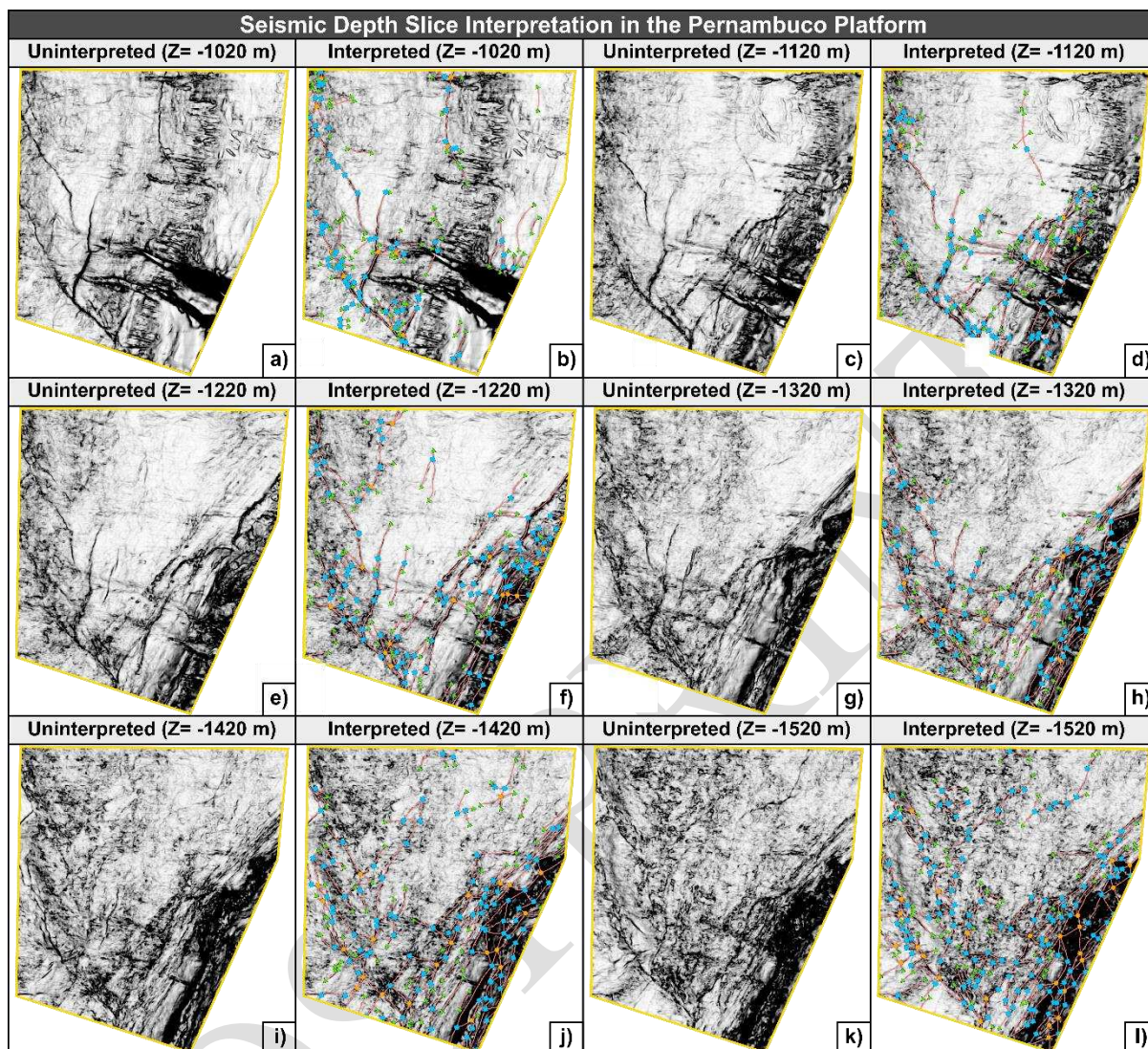






1315

Figure 8



1316

1317

1318

1319

1320

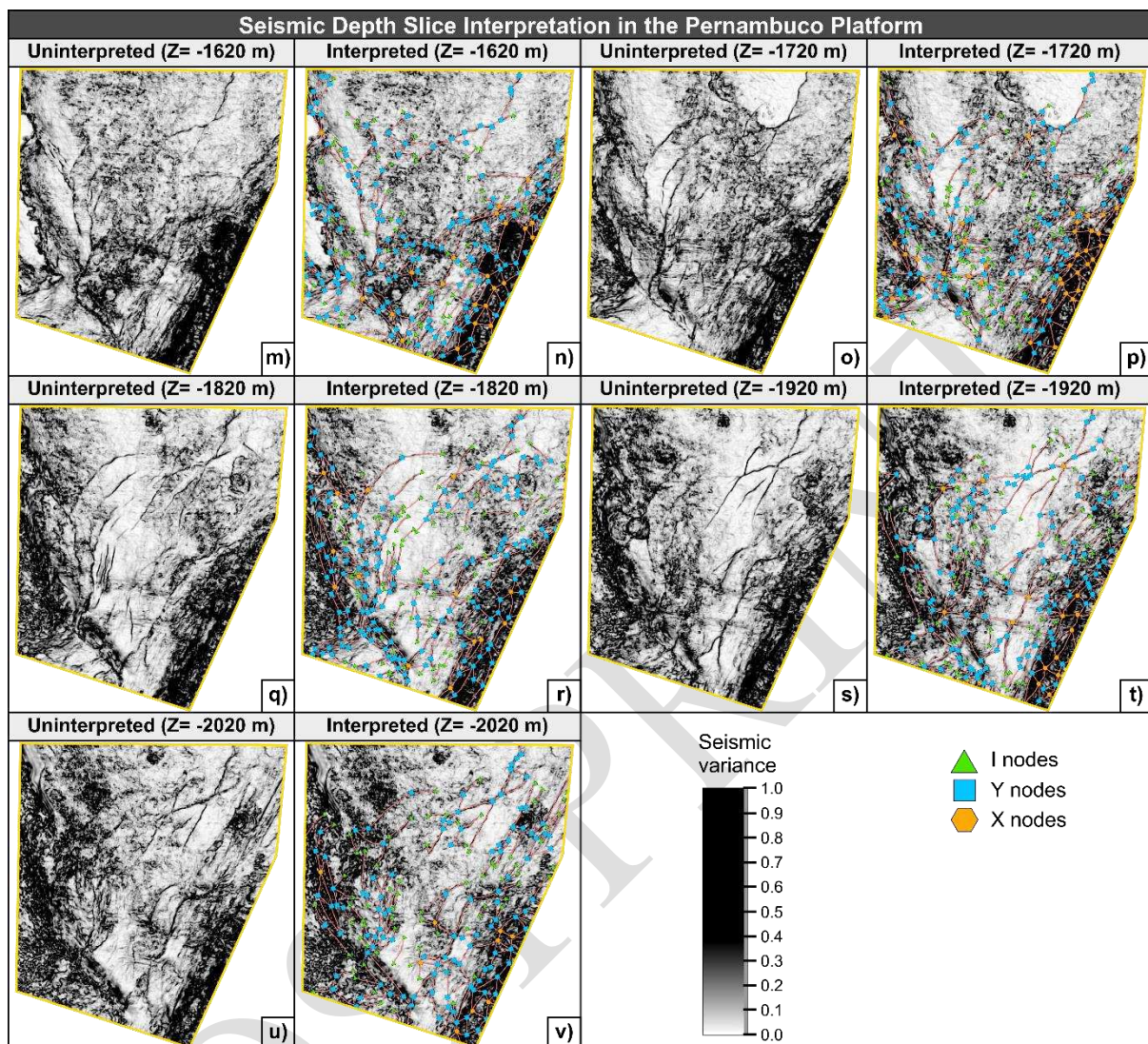
1321

1322

1323

1324

Figure 8. Continued



1325

1326

1327

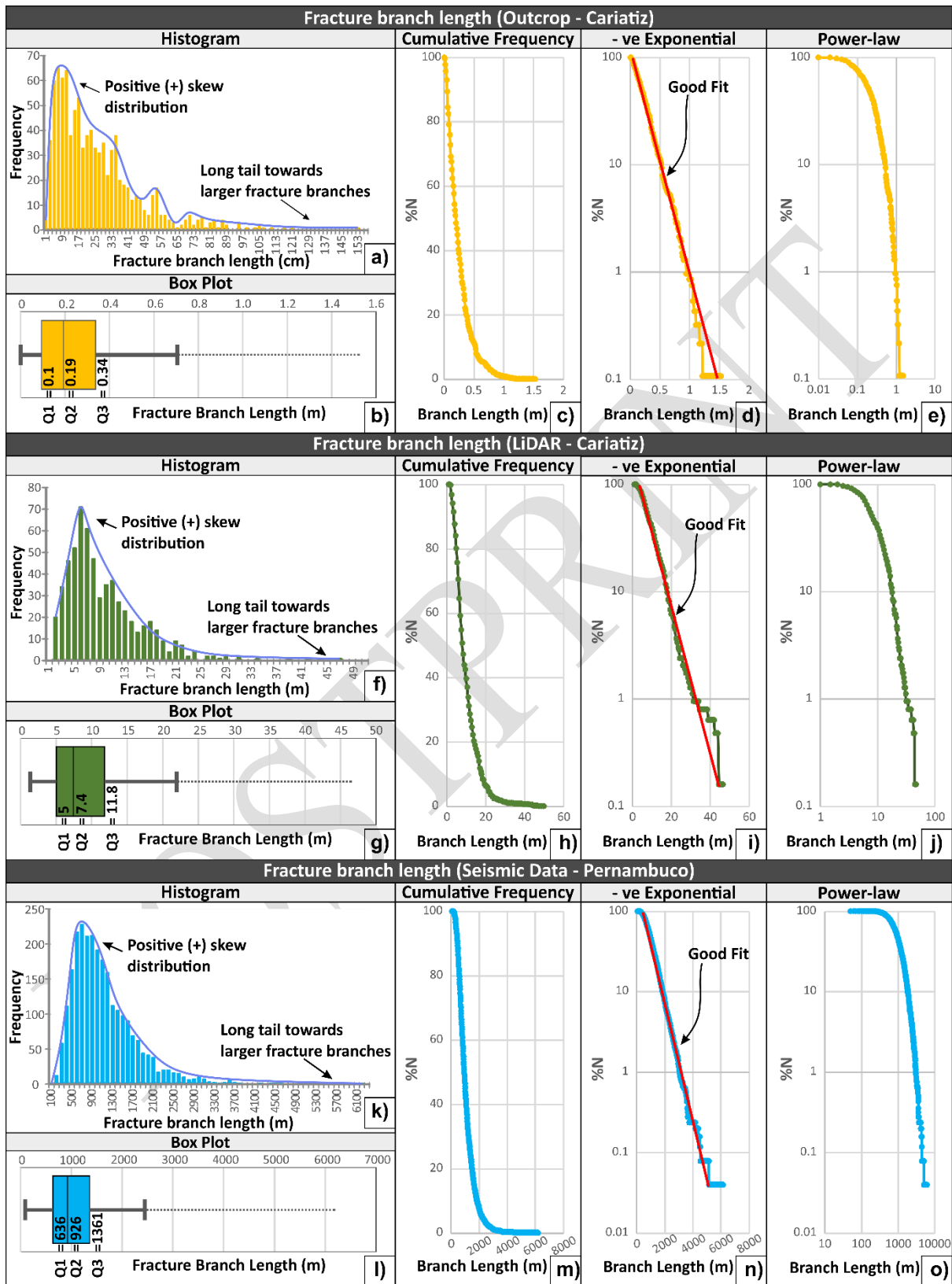
1328

1329

1330

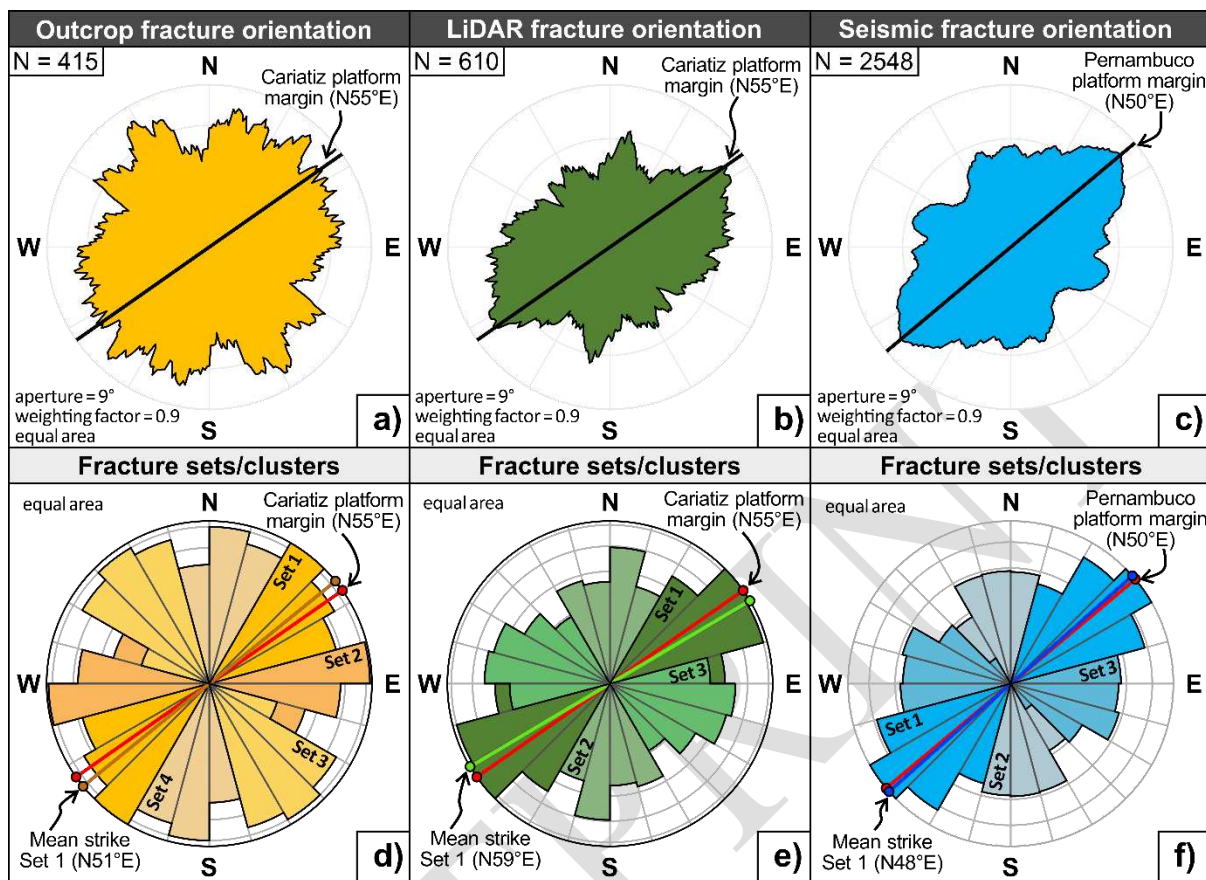
1331

1332



1336

Figure 10



1337

1338

1339

1340

1341

1342

1343

1344

1345

1346

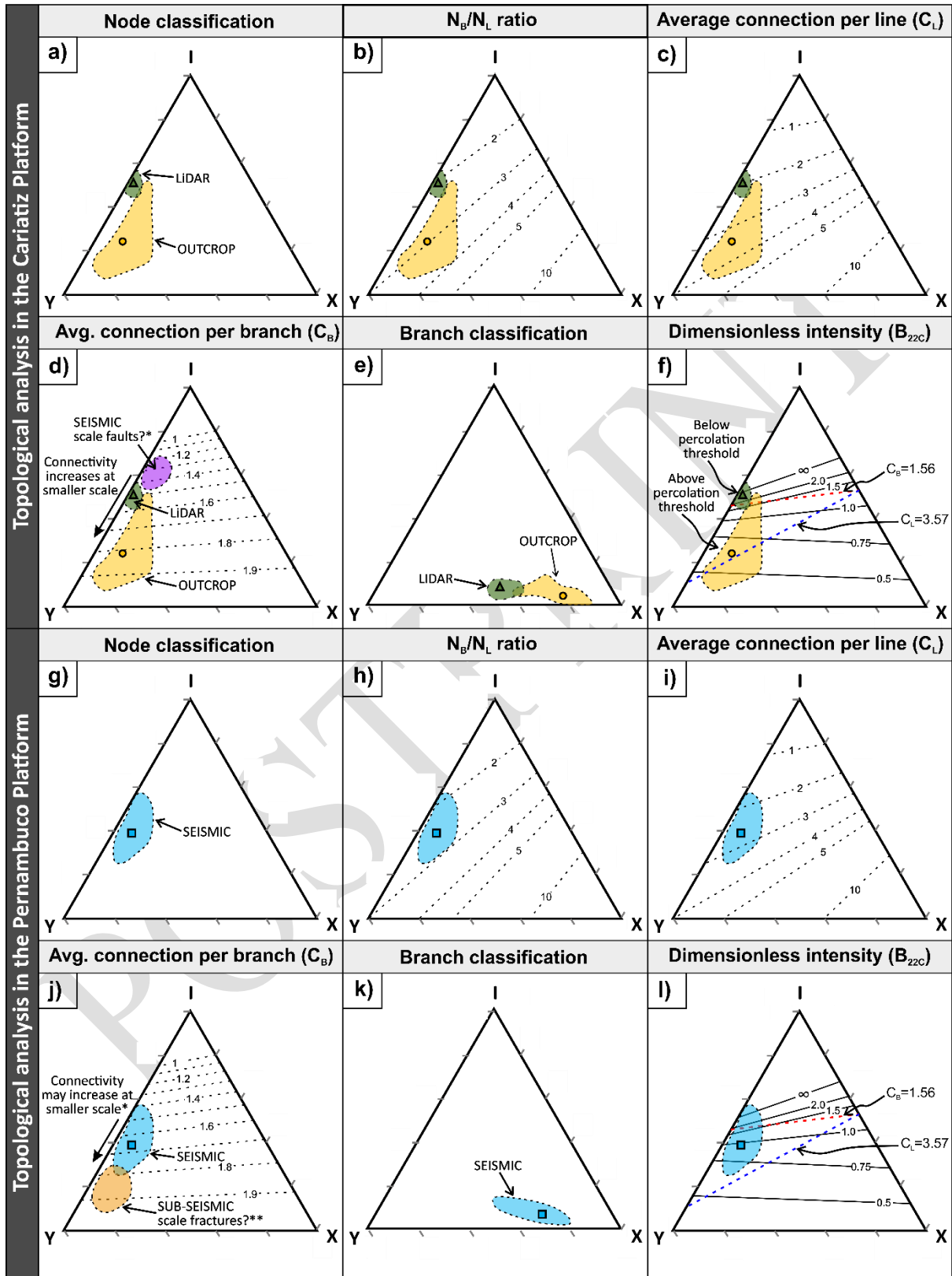
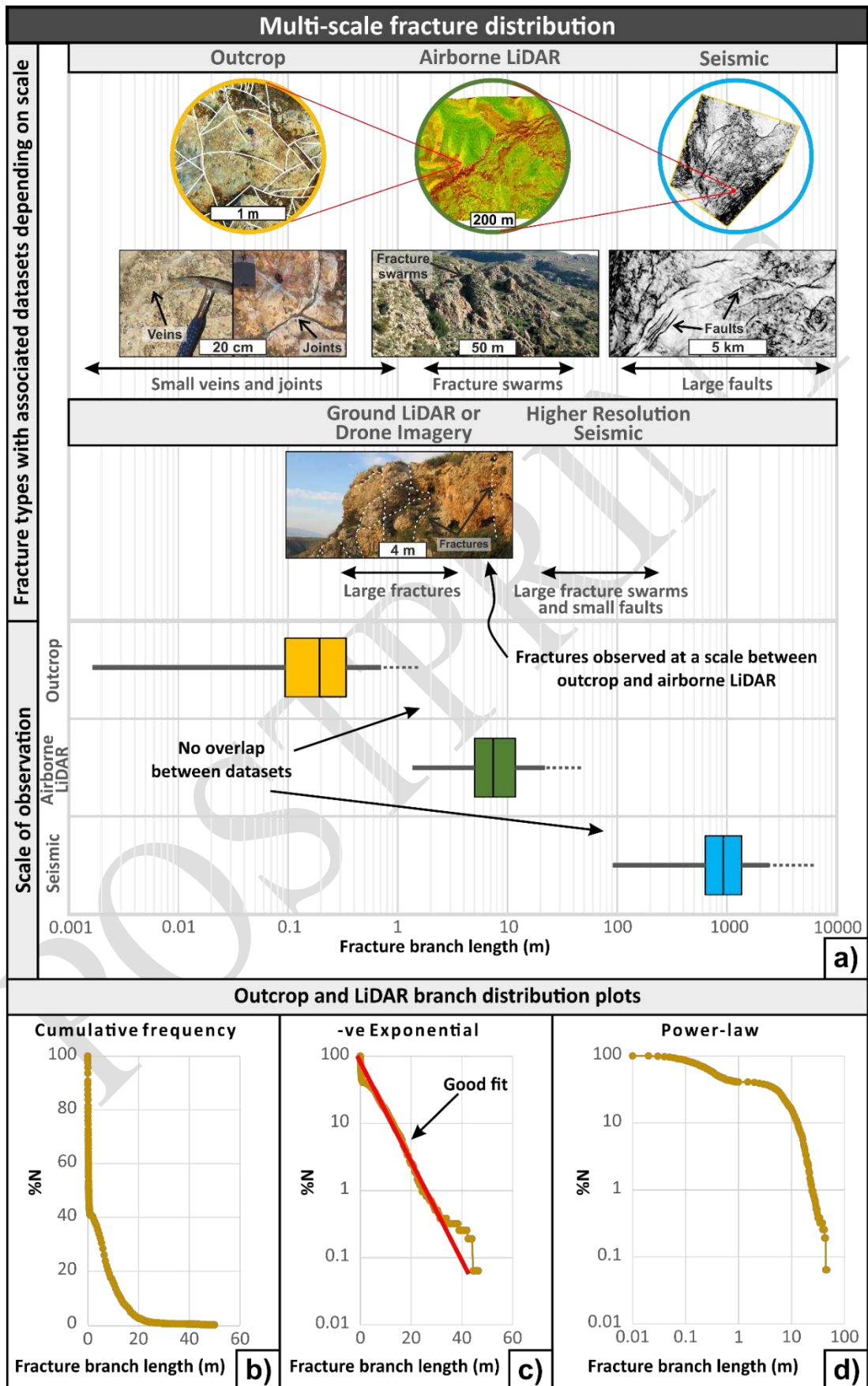


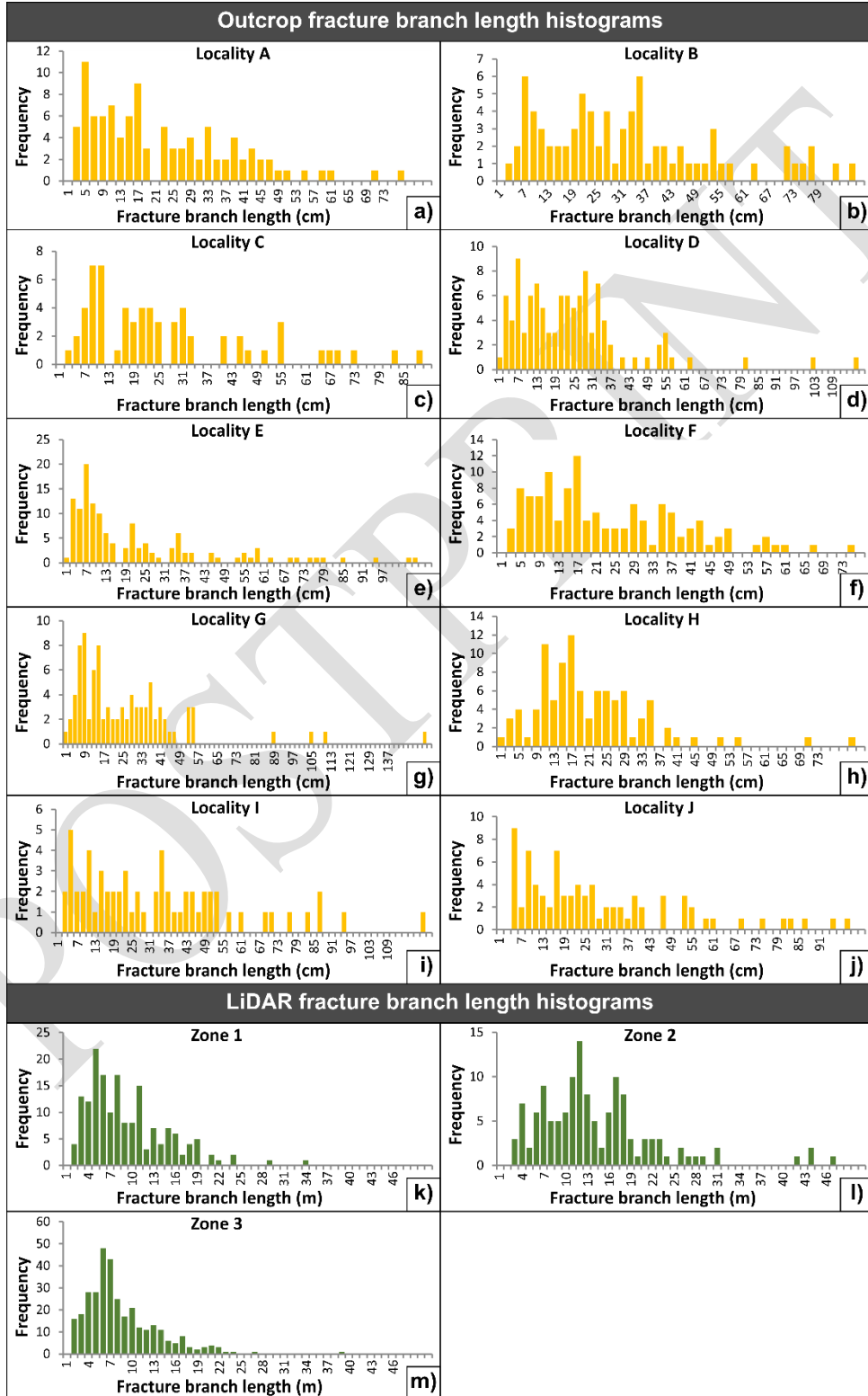
Figure 12



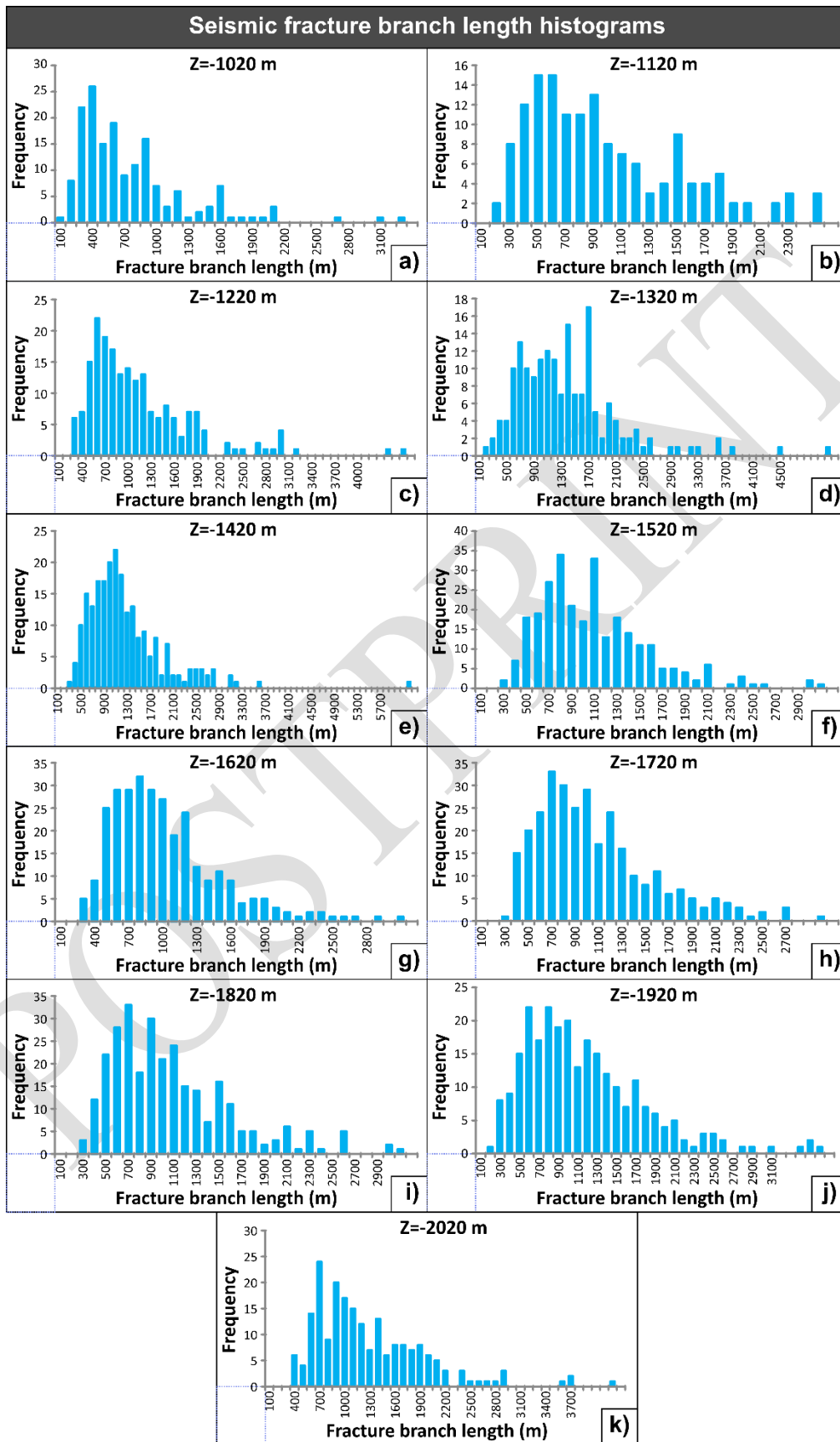
1352 12 Supplementary data

1353 Appendix A. Fracture branch length distribution histograms

1354 Figure A1

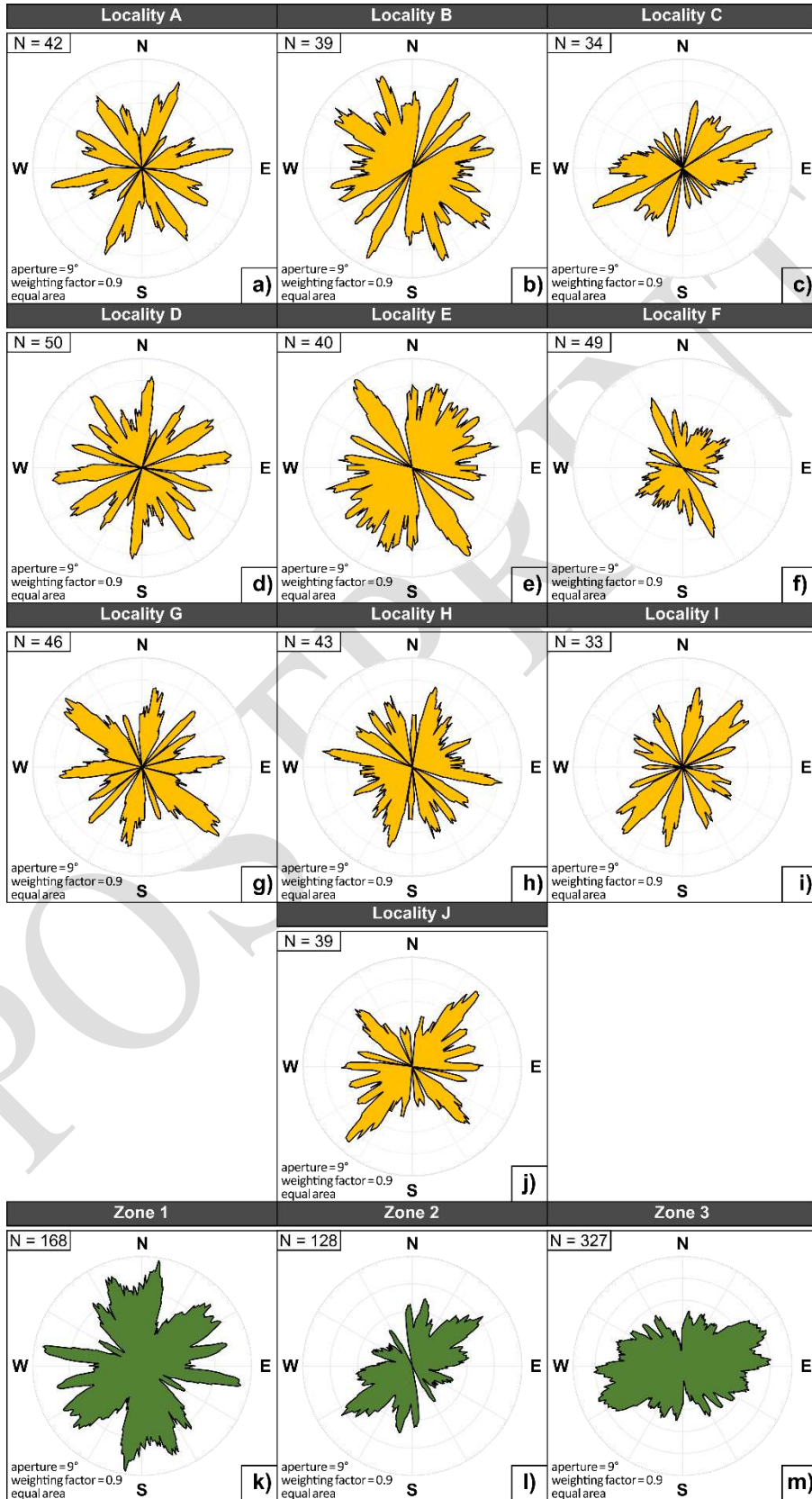


1355



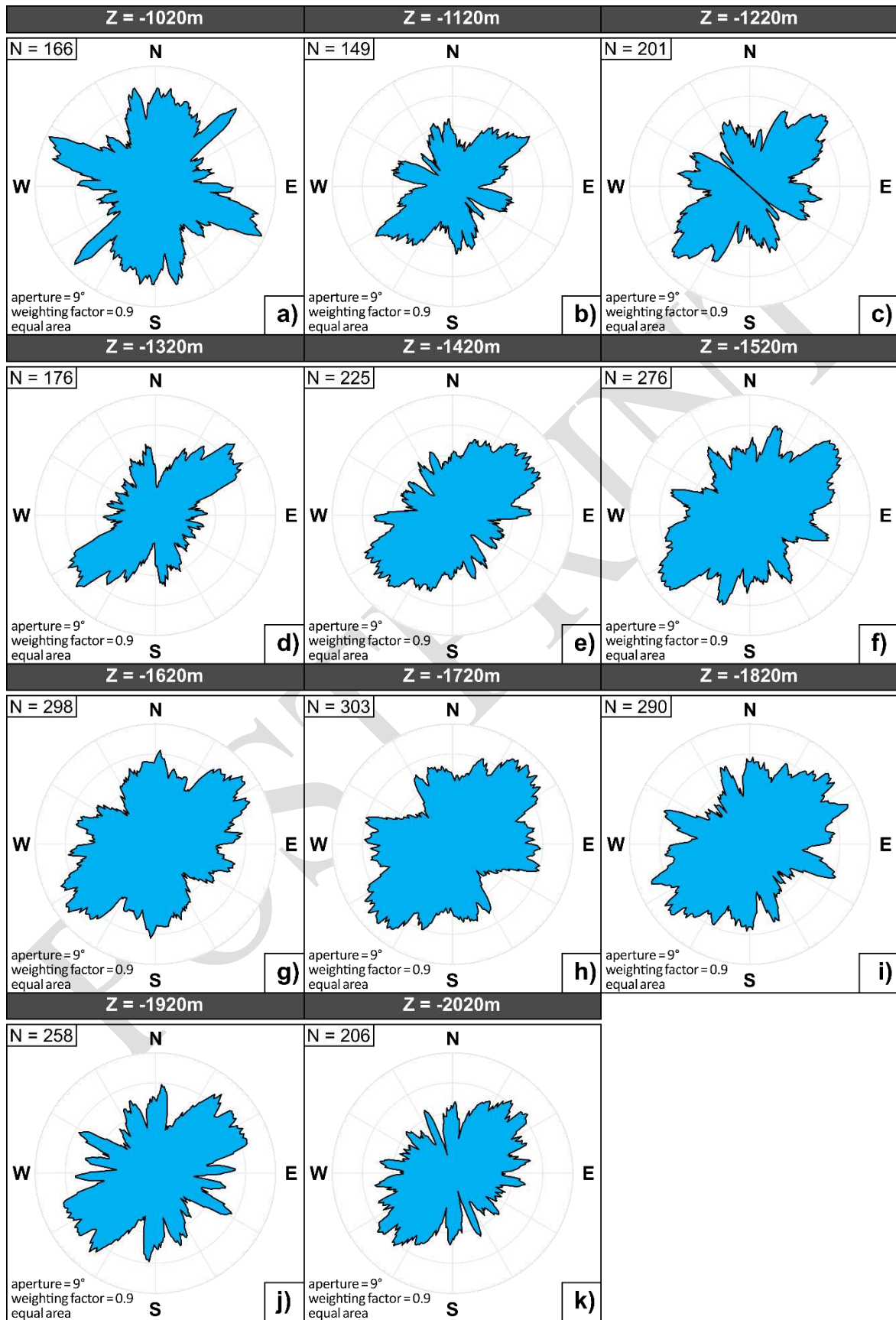
1359

Figure B1

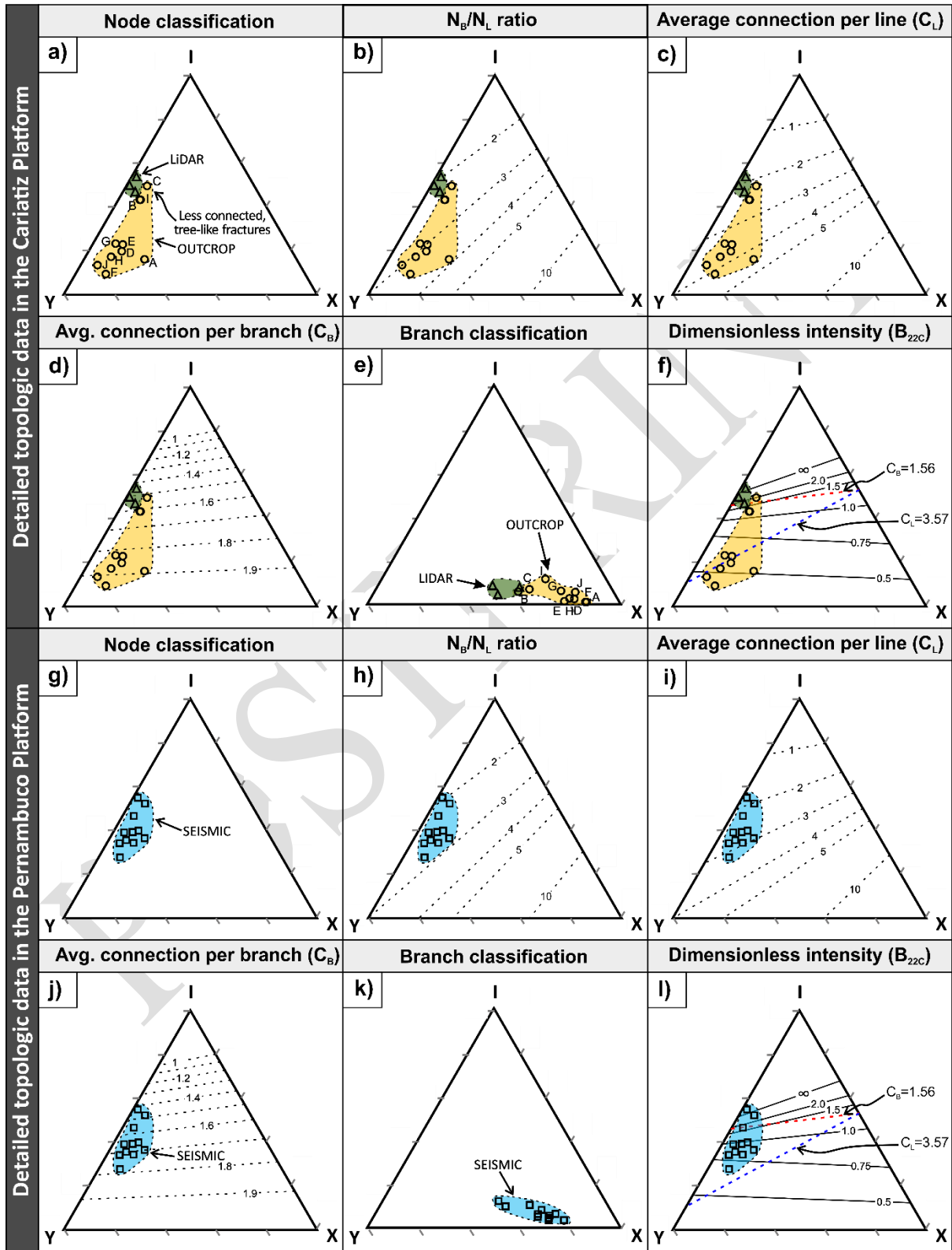


1360

Figure B2



1364 Figure C1



1366 Appendix D. Fracture topological data

1367 Table D1

Parameter	Notation	Equations
Nodes	I, Y, X	Isolated, abutting or splaying, crossing
Number of nodes	N_I, N_Y, N_X	
Branches	$I-I, I-C, C-C$	Isolated, singly-, doubly-connected
Total nodes	N_N	$N_N = N_I + N_Y + N_X$
Total lines	N_L	$N_L = (N_I + N_Y) / 2$
Total branches	N_B	$N_B = (N_I + 3N_Y + 4N_X) / 2$
Branches/Lines	N_B / N_L	$N_B / N_L = (N_I + 3N_Y + 4N_X) / (N_I + N_Y)$
Average connections/line	C_L	$C_L = 2 (N_Y + N_X) / N_L$
Average connections/branch	C_B	$C_B = (3N_Y + 4N_X) / N_B$
Branch dimensionless intensity at percolation	B_{22C}	
Probability of isolated nodes	P_I	$P_I = N_I / (N_I + 3N_Y + 4N_X)$
Prob. connected nodes	P_C	$P_C = (3N_Y + 4N_X) / (N_I + 3N_Y + 4N_X)$
Prob. of isolated branches	P_{II}	$P_{II} = P_I^2$
Prob. of singly connected branches	P_{IC}	$P_{IC} = P_I P_C$
Prob. of doubly connected branches	P_{CC}	$P_{CC} = P_C^2$

1368

1369

1370

1371

1372

1373

1374

1375

1376

1377

1378

1379

1380

	Node count			Branch count			Number of lines or traces (NL)	Number of branches (NB)	Number of branches to traces ratio (NB/NL)	Total fracture length (FLT)	Average trace length (LL)	Average branch length (BL)	Connections per line or trace (CL)	Connections per branch (CB)	Proportion of nodes		Proportion of branches		
	NI	NY	NX	I-I	I-C	C-C									Isolated (PI)	Connected (PC)	Isolated (PII)	Singly connected (PIC)	Doubly connected (PCC)
Field data (Outcrop)										[cm]	[cm]	[cm]							
Site A	9	36	14	0	13	86	22.5	86.5	3.84	2232.17	99.21	25.81	4.44	1.90	0.0520	0.9480	0.0027	0.0493	0.8987
Site B	26	30	5	4	30	45	28	68	2.43	2436.43	87.02	35.83	2.50	1.62	0.1912	0.8088	0.0365	0.1546	0.6542
Site C	25	22	4	4	21	39	23.5	53.5	2.28	1661.31	70.69	31.05	2.21	1.53	0.2336	0.7664	0.0546	0.1791	0.5873
Site D	12	43	8	2	18	87	27.5	86.5	3.15	2519.18	91.61	29.12	3.71	1.86	0.0694	0.9306	0.0048	0.0646	0.8661
Site E	19	57	10	1	27	98	38	115	3.03	2761.9	72.68	24.02	3.53	1.83	0.0826	0.9174	0.0068	0.0758	0.8416
Site F	6	56	8	0	16	104	31	103	3.32	2749.91	88.71	26.70	4.13	1.94	0.0291	0.9709	0.0008	0.0283	0.9426
Site G	13	40	5	5	18	66	26.5	76.5	2.89	2357.84	88.98	30.82	3.40	1.83	0.0850	0.9150	0.0072	0.0777	0.8373
Site H	10	45	6	2	18	76	27.5	84.5	3.07	1999.34	72.70	23.66	3.71	1.88	0.0592	0.9408	0.0035	0.0557	0.8852
Site I	20	23	4	7	15	41	21.5	52.5	2.44	2096.67	97.52	39.94	2.51	1.62	0.1905	0.8095	0.0363	0.1542	0.6553
Site J	6	39	3	4	12	65	22.5	67.5	3.00	2250.83	100.04	33.35	3.73	1.91	0.0444	0.9556	0.0020	0.0425	0.9131
All outcrop	146	391	67	29	188	707	268.5	793.5	2.96	23065.58	85.91	29.07	3.41	1.82	0.0920	0.9080	0.0085	0.0835	0.8245
Field data (Lidar)										[m]	[m]	[m]							
Zone 1	83	87	8	12	60	92	85	188	2.21	1507.81	17.74	8.02	2.24	1.56	0.2207	0.7793	0.0487	0.1720	0.6072
Zone 2	74	74	0	6	63	66	74	148	2.00	1791.94	24.22	12.11	2.00	1.50	0.2500	0.7500	0.0625	0.1875	0.5625
Zone 3	207	175	6	28	153	147	191	378	1.98	2633.2	13.79	6.97	1.90	1.45	0.2738	0.7262	0.0750	0.1988	0.5274
Lidar	364	336	14	46	276	305	350	714	2.04	5932.95	16.95	8.31	2.00	1.49	0.2549	0.7451	0.0650	0.1899	0.5552
Seismic data										[m]	[m]	[m]							
-1020 m	97	78	11	15	67	83	87.5	187.5	2.14	119340.04	1363.89	636.48	2.03	1.48	0.2587	0.7413	0.0669	0.1918	0.5496
-1120 m	96	76	3	17	62	68	86	168	1.95	139308.08	1619.86	829.21	1.84	1.43	0.2857	0.7143	0.0816	0.2041	0.5102
-1220 m	78	106	15	9	60	132	92	228	2.48	220090.82	2392.29	965.31	2.63	1.66	0.1711	0.8289	0.0293	0.1418	0.6872
-1320 m	87	92	8	17	53	104	89.5	197.5	2.21	234830.78	2623.81	1189.02	2.23	1.56	0.2203	0.7797	0.0485	0.1717	0.6080
-1420 m	88	112	21	12	65	145	100	254	2.54	275457.57	2754.58	1084.48	2.66	1.65	0.1732	0.8268	0.0300	0.1432	0.6836
-1520 m	89	144	27	8	73	195	116.5	314.5	2.70	286638.22	2460.41	911.41	2.94	1.72	0.1415	0.8585	0.0200	0.1215	0.7370
-1620 m	76	176	23	8	60	228	126	348	2.76	288439.9	2289.21	828.85	3.16	1.78	0.1092	0.8908	0.0119	0.0973	0.7935
-1720 m	101	139	38	12	78	212	120	335	2.79	308308.35	2569.24	920.32	2.95	1.70	0.1507	0.8493	0.0227	0.1280	0.7212
-1820 m	95	170	14	16	64	208	132.5	330.5	2.49	296778.68	2239.84	897.97	2.78	1.71	0.1437	0.8563	0.0207	0.1231	0.7332
-1920 m	88	143	17	12	64	180	115.5	292.5	2.53	287458.13	2488.81	982.76	2.77	1.70	0.1504	0.8496	0.0226	0.1278	0.7218
-2020 m	84	122	9	15	54	132	103	243	2.36	254034.02	2466.35	1045.41	2.54	1.65	0.1728	0.8272	0.0299	0.1430	0.6842
All seismic	979	1358	186	141	700	1687	1168.5	2898.5	2.48	2710684.59	2319.80	935.20	2.64	1.66	0.1689	0.8311	0.0285	0.1404	0.6908

Table D2

POSTPRINT